

LUCAS NUNES LOPES

**Forward track reconstruction and quality
assessment for the ALICE experiment of
the Large Hadron Collider**



PORTE ALEGRE, RS - Brazil
October, 2022

**FORWARD TRACK RECONSTRUCTION AND QUALITY
ASSESSMENT FOR THE ALICE EXPERIMENT OF THE
LARGE HADRON COLLIDER**

Lucas Nunes Lopes

This master's degree dissertation was written under supervision of Prof. Dr. Rafael Peretti Pezzi and Prof. Dr. Luis Gustavo Pereira, and it was submitted to the Physics Institute of the Federal University of Rio Grande do Sul as a requirement for obtaining the Master's degree.

Federal University of Rio Grande do Sul
Physics Institute

Supervisor: Prof. Dr. Rafael Peretti Pezzi
Co-supervisor: Prof. Dr. Luis Gustavo Pereira

Porto Alegre, RS - Brasil
October, 2022

RECONSTRUÇÃO DE TRILHAS FRONTAIS E AVALIAÇÃO DE QUALIDADE PARA O EXPERIMENTO ALICE DO GRANDE COLISOR DE HADRONS

Lucas Nunes Lopes

Dissertação escrita sob supervisão do Prof. Dr. Rafael Peretti Pezzi e Prof. Dr. Luis Gustavo Pereira, e apresentada ao Instituto de Física da Universidade Federal do Rio Grande do Sul como requisito parcial para a obtenção do título de Mestre em Física.

Universidade Federal do Rio Grande do Sul
Instituto de Física
Programa de Pós-Graduação em Física

Orientador: Prof. Dr. Rafael Peretti Pezzi
Co-orientador: Prof. Dr. Luis Gustavo Pereira

Porto Alegre, RS - Brasil
Outubro de 2022

Acknowledgements

First, and always first, I would like to acknowledge my parents and all my family for the ever-lasting support.

The gratitude is also extended to those who, although without blood ties, are always in my thoughts.

In special to my girlfriend, Fernanda, whom, with the unlimited support, life-saving lessons and unyielding love, helped me through this stage of my life.

To Prof. Rafael Pezzi for his guidance, teachings and patience during this project.

To Prof. Luis Gustavo for his contributions and key aid in the writing process.

To Prof. Maria Beatriz Gay Ducati and GEFAE group, for the work opportunity.

To Prof. Lucas Schnorr, for providing access to High-Performance Computing Park and also for the, although few, rich discussions.

To Dr. Stefano Mathias Panebianco, for the opportunity at the MFT project and to know ALICE, and for the wise advices.

To all the “MFTeam”, who warm welcomed me in my stay at CERN.

To my friends and colleagues, who contribute to my knowledge and made the last few months of work feel more real.

And to all who contributed in some way to my formation, my sincerely thanks.

Moreover, I thank the Federal University of Rio Grande do Sul (UFRGS) and the Physics Institute of UFRGS.

To CAPES, who has funded this master’s project.

And to FAPERGS, for the financial support in my travel to CERN, through the project number 19/2551-0001746-4.

*“No man is brave that has never walked a hundred miles.
If you want to know the truth of who you are, walk until
not a person knows your name. Travel is the great leveler;
the great teacher, bitter as medicine, crueler than
mirror-glass. A long stretch of road will teach you more
about yourself than a hundred years of quiet.”*

Patrick Rothfuss, The Wise Man's Fear

Abstract

The ALICE experiment is one of the 4 largest experiments at CERN’s LHC and has the main goal of characterizing the physical properties of the Quark-Gluon Plasma, the state of the universe before the creation of baryonic matter, created under extreme conditions of temperature and energy density. This state can be observed by ALICE when produced by ultra-relativistic heavy ion collisions. In order to be prepared for LHC’s third round of data taking (RUN 3), ALICE has undergone several upgrades, which included the installation of the Muon Forward Tracker detector (MFT). MFT installation aims at improve vertexing resolution, in order to clarify the origin of muons seen by ALICE’s muon spectrometer. In modern particle detectors, the physics analysis from detector observations can only be executed after the computational track reconstruction of the particles trajectory. This work presents a study of particle-track reconstruction and its application to the Muon Forward Detector. Several track models (namely the helix model and its first and second order approximations) and fitting methods (Kalman Filter and χ^2 -minimization) were used in track reconstruction. The reconstruction performance of each case was evaluated through the vertex and *momentum* resolutions and track-parameters errors. In addition to that, experiment parameters of sensor resolution and material budget are also addressed in the reconstruction assessment. Results presented here justify the track-reconstruction strategy adopted by MFT for RUN 3. The developed algorithms used in this work were uploaded in ALICE online-offline computing system and are already in use during RUN 3 of the LHC.

Key-words: Tracking, particle physics, MFT detector.

Resumo

O experimento ALICE é um dos quatro grandes experimentos no Grande Colisor de Hadrons (LHC) do CERN (Centro Europeu de Pesquisas Nucleares) e tem como principal objetivo caracterizar as propriedades do Plasma de Quark e Gluons, estado em que o universo se encontrava antes da criação da matéria bariônica, criado sob condições extremas de temperatura e densidade de energia. Esse estado da matéria pode ser observado por ALICE a partir de colisões ultrarrelativísticas de íons pesados. Para se preparar para a terceira tomada de dados do LHC (RUN 3), ALICE passou por uma série de upgrades, dentre os quais estava a instalação do novo detector frontal de muons (MFT, do inglês *Muon Forward Tracker*). O MFT tem como objetivo melhorar a resolução de vértice, com o intuito de tornar mais precisa a definição das origens dos muons observados pelo espectrômetro de muons de ALICE. Nos detectores modernos, a análise física proveniente das observações de um detector apenas pode ser feita depois da reconstrução computacional das trajetórias das partículas. Este trabalho apresenta um estudo sobre a reconstrução de trajetórias de partículas com aplicação para o MFT. Diferentes modelos de trilhas (a saber, modelo de hélice e suas aproximações em primeira e segunda ordem) e métodos de ajuste (Filtro de Kalman e minimização de χ^2) foram usados na reconstrução de trilhas e o desempenho de cada caso foi avaliado analisando as resoluções de vértice e *momentum*, e os erros dos parâmetros referentes à trilha reconstruída. Ainda, os impactos de parâmetros experimentais referentes à resolução do sensor e quantidade de material do mesmo na reconstrução também foram avaliados. Os resultados aqui apresentados justificam a escolha da estratégia de reconstrução do MFT adotada no RUN 3. Os algoritmos desenvolvimentos foram integrados no sistema computacional de ALICE e já estão em uso no RUN 3 do LHC.

Palavras-chave: Física de partículas, rastreamento de trajetórias, detector MFT.

Contents

1	Introduction	1
1.1	Particle physics	1
1.1.1	Key particle detection technologies	2
1.1.2	Particle-track reconstruction	6
1.2	The A Large Ion Collider Experiment	7
1.2.1	Scientific program of ALICE	8
1.2.2	The Muon Spectrometer	9
1.2.3	The Muon Forward Tracker	11
1.3	Objectives of this project	12
2	Theoretical and methodological approach	14
2.1	Particle-track reconstruction	14
2.1.1	Track models	15
2.1.1.1	Multiple Coulomb Scattering effects	21
2.1.2	Track-parameter and uncertainties	22
2.1.3	Track fitting	26
2.1.3.1	χ^2 -minimization	26
2.1.3.2	Kalman Filter	28
2.2	Quality control of reconstructed track parameters	31
2.2.1	Computational tools	33
3	Development, results and discussion	35
3.1	Simulation and reconstruction	36
3.2	Assessment of track-reconstruction	36
3.3	Results	38
3.3.1	Comparisons of track models and fitting methods	38
3.3.1.1	Comparison between helix track model and approximations .	38

3.3.1.2	Fitting methods: Kalman Filter and χ^2 -minimization	40
3.3.2	Experiment parameters	42
3.3.2.1	Cluster topology resolution effects	42
3.3.2.2	Material budget effects	43
3.3.2.3	Other event topologies	45
4	Conclusion	47
A	Track finding in the Muon Forward Tracker	52
B	Transformations between MFT and MCH coordinate systems	53
Acronyms		63
Glossary		65

CHAPTER 1

INTRODUCTION

The *Large Hadron Collider* (LHC) is the world's largest particle collider, located at the border between France and Switzerland. The LHC consists of a 27 km circumference ring, where two particle beams travel in opposite directions and can collide with energies up to 13 TeV for proton-proton (pp) collisions or 5.5 TeV for lead-lead (Pb-Pb) collisions. One of the collision points is located at the *A Large Ion Collider Experiment* (ALICE), which studies the *Quark-Gluon Plasma*, the state in which it is believed the universe was around 10^{-10} s to 10^{-6} s after the Big Bang. This state can only be reproduced in extremes conditions of temperature and energy density, which are achieved through nuclear Pb-Pb collisions. The ALICE experiment has been upgraded recently, aiming to improve spacial and timing resolutions. As a part of the upgrade, the Muon Forward Tracker (MFT), a new detector in frontal geometry, was installed with the goal of improving vertexing resolution of ALICE's muon spectrometer.

This work aims at studying particle-track reconstruction methods suitable for forward geometries and its application to the MFT detector, seeking to assess the reconstructed tracks with tools developed and then implemented within MFT reconstruction workflow.

Studies of track models capable of describing charged particle trajectories and track-fitting methods were performed. In order to assess the quality of reconstructed track-parameters and carry out the study, the transverse offset and transverse *momentum* resolution and their respective normalized residuals (pulls) were analysed as functions of the transverse *momentum*. Regarding track models, the resolutions and pulls of the theoretical helix model and its second and first order approximation were compared. For track fitting methods, comparisons between track-reconstruction using the Kalman Filter and χ^2 -minimization were realised. In addition to that, the impact of sensor resolution and material budget were also evaluated.

This dissertation is organized as follows: chapter 1 presents a brief overview of tracking detectors and track reconstruction concepts, alongside with a presentation of the ALICE experiment, its muon spectrometer and the new Muon Forward Tracker detector. Chapter 2 presents the necessary theoretical background and methods used in this work. Chapter 3 contains the work implementation, followed by the achieved results¹ and discussion regarding it.

1.1 Particle physics

Particle Physics is the branch of physics which studies the fundamental constituents of matter and radiation, and their interactions. Since many of these fundamental particles can

¹The results shown here have a preliminary status, not representing official performances of the MFT.

only be created in significant quantities using high energy experiments, this field is also known as High Energy Physics. The dominant theory in the field is the Standard Model, which can explain almost every experimental results obtained in modern times. For instance, this theory has successfully predicted the existence of the W, Z and Higgs bosons, the gluon and the top and charm quarks.

Particle Physics made important contributions to elucidate our understanding of the universe. Among those we can cite the discoveries of the electron (1897) [1], positron (1932) [2], muon (1936) [3], pion (1947) [4] and more recently, the W and Z bosons (1983) [5, 6, 7] and the Higgs boson (2012) [8]. By pushing the limits of the experiments capabilities further and further, the field is a driving force in the development of new technologies. One example of this is the imaging technique of positron emission tomography (PET), widely used in medicine. One can also cite the creation of the World Wide Web at CERN, as a product of the scientific development.

The electron was the first subatomic particle to be discovered. In 1897 J. J. Thomson used cathode rays to estimate the electron charge and mass. A precise measurement of the electron charge and mass was made in 1909 by Robert Millikan and Harvey Fletcher with an oil drop experiment. The development of experiments looking for more precise measurements and new particles did not stop and soon after the Cloud Chamber used in the positron discovery was designed. In order to continue and investigate even further the matter constituents, detection technologies also advance and today it allows us to glimpse the first moments of the universe.

Nowadays, new discoveries in particle physics require significant advances in experimental setups, data processing, analysis software and computing infrastructure. The next subsection highlights key particle detection technologies developed during the last century in order to contextualize the data taking of particle tracker detectors. Next, we present an overview of Track Reconstruction concepts, which is a central element of this work. This topic is addressed in more details in section 2.1.

1.1.1 Key particle detection technologies

This section presents key particle detection technologies, organized in two parts. At first, photography-based methods are presented, followed by methods that resulted in much higher event processing rates with electronic readout.

Photograph-based detectors: By means of photography it was possible to record observations of the trail left by an ionizing particle. The main disadvantage was the limited data rate. Physical analysis could only begin after image processing, which, together with chamber preparation consumed a long time.

- Cloud/bubble chamber:
 - Cloud and bubble chambers are based on supersaturated and meta-stable fluids where the passage of charged particles creates a visible trail in the medium by condensing the medium ions around it (see figure 1). They were used in the discoveries of positron (Cloud-Chamber, 1932); muon (Cloud-Chamber, 1936) and neutral current (Z bosons interactions, 1973).
- Nuclear Emulsions:

- Nuclear Emulsion is a detector based on photographic film. The emulsion is made mostly of micro crystal of silver embedded in gelatine. The spatial resolution is extremely precise, of the order of a few μm , even compared with modern detectors. It was used in the discovery of the pion, after a key improvement by César Lattes, who ordered emulsions with boron added to the gelatin [9].

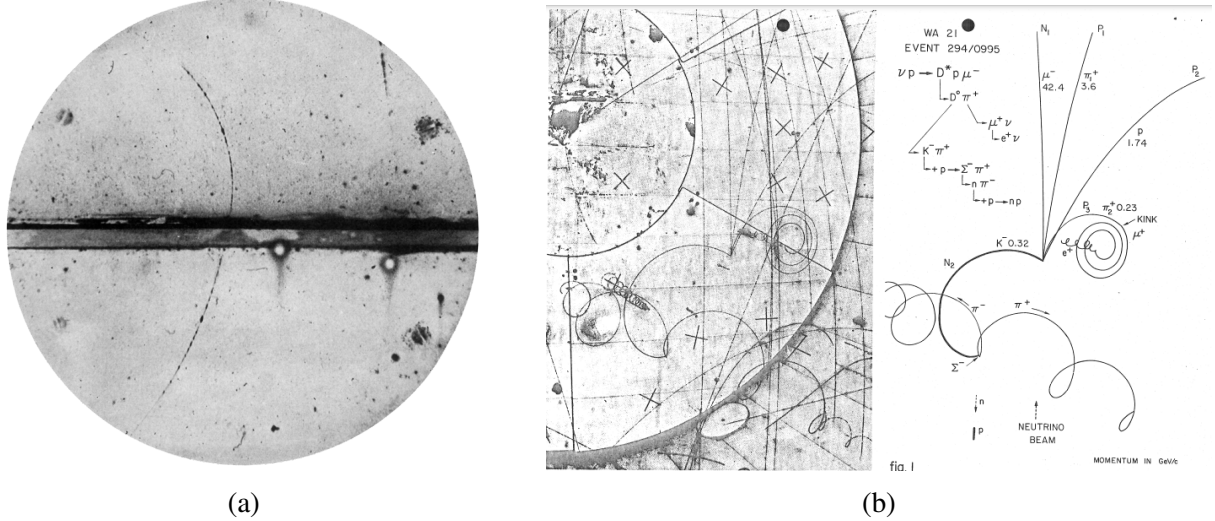


Figure 1: a) Image of trail left by a positron in a cloud chamber [2]. b) record of production and decay of the D-meson with the use of a bubble chamber [10].

Electronic readout: technology evolution lead to electronic readout methods, where sensor signals are automatically processed and recorded by electronic circuits, leading to a much faster data taking. Some well-known gaseous detectors, as well as modern silicon detectors enters into this category. Signal in gaseous detectors are produced by ionized electrons resulting from a particle passing through an ionizing gas. Most modern solid state particle detectors explore the properties of semiconductor P-N junctions and are usually made of silicon. The passage of charged particles generate electron-hole pairs which are collected by electrodes, generating a detectable electronic signal. A review of the working principles of these type of detectors can be found in chapter 7 of [11]. Detectors that can be considered milestones in the evolution of the field are summarized below.

- Geiger-Müller counter
 - Geiger-Muller tubes are one of the simplest gaseous detectors. These tubes use a single wire as an anode to attract electrons and generate the signal. It is not able to differentiate radiation, as signals have always the same magnitude, due to its working principle based on avalanche ionization. As it has only one wire, it cannot determine the position of a particle.
- Multi-wire proportional chamber (MWPC)
 - Multi-wire proportional chambers are formed by arrays of wires which provide information about the position of the particles. In practice these were the first electronic particle-tracking detectors. It was a great upgrade from previous devices, as it could reach a spatial resolution of 0.3 mm and handle higher fluxes.

- Drift chamber
 - Drift chambers exploits the drift velocity of ion tracks left by the passage of charged particles. It combines time and position measurements to obtain the distance that the particle passed from the wires, resulting in a resolution between 0.1 mm and 3 mm.
- Time-Projection Chamber (TPC)
 - The TPC is a gas filled-chamber, with MWPC as end-caps detectors, capable of 3D spatial measurements with resolution of the order of 1 mm to 0.1 mm, plus a time measurement. Currently in use in many particle physics experiments; display of a Pb-Pb collision at ALICE's TPC can be seen in figure 2.
- Micro-pattern gas detectors
 - Micro-pattern gas detectors have the same working principle of the MWPC, where the wires are replaced by microscopic strip structures deposited on high-resistivity substrates. These structures can be separated in smaller distances, resulting in a spatial resolution below 20 μm . The Gas Electron Multiplier belongs to this group of detectors and can be used as end-caps in TPC in order to achieve better resolutions.
- Silicon strips:
 - One way to segment electrodes in solid state detectors is in the form of silicon strips. The strips have a typical width of 20 μm and a typical distance from each other of 100 μm [12, chapter 1]. 2D measurements can be achieved using two non-parallel sets of strips. Spatial resolution of 10 μm or better can be achieved.
- Hybrid pixel detectors:
 - In hybrid pixel detectors the pixel sensor and the readout chip are combined in one piece of silicon. They can deal better with a high track density environment than strips and are better suitable to separate the primary vertex from secondary vertices, reaching a spatial resolution lower than 10 μm .
- Monolithic Active Pixel Sensor (MAPS)
 - Monolithic Active Pixel Sensor consists of a pixel matrix embedded in single silicon chip together with its analog and digital signal processing electronics. MAPS are made using Complementary metal-oxide semiconductor (CMOS) technology and are compact and low cost as compared to previous technologies. While retaining a good resolution, the lesser amount of material gives a lower material budget, reducing the interaction with matter e.g. multiple scattering effects.
 - ALICE PIxel DEtector (ALPIDE): ALPIDE is a MAPS development used in the ALICE upgrade, namely in the new Inner Tracking System and in the new Muon Forward Detector. The chip measures 1.5 cm \times 3 cm and has more than 500 thousand pixels of 28 μm \times 28 μm distributed in 512 rows and 1024 columns. It was designed to have an asynchronous readout and very low power consumption. ALPIDE can achieve a spatial resolution of about 5 μm . More on ALPIDE's principle of operation, performance and characteristics can be found in [13, 14].

Detector type	Spatial resolution	Dead time
Bubble chamber	10-150 μm	50 ms
Proportional chamber (MWPC)	50-100 μm	20-200 ns
Drift Chamber	50-100 μm	20-100 ns
Micro-pattern gas detector	30-40 μm	10-100 ns
Silicon strip	pitch/(3 to 7) μm	\lesssim 50 ns
Silicon pixel	\lesssim 10 μm	\lesssim 50 ns
Emulsion	1 μm	–

Table 1: Typical resolutions and dead-times of common charged particle detectors. Adapted from [15].

Table 1 was adapted from the Particle Data Group review on particle detectors [15] and shows the resolutions and dead-time (time after detection when the sensor is not able to receive new signals) for some of the mentioned detectors.

The advances in detection technologies were fundamental to achieve the level of precision of current collider experiments. At the LHC, protons are colliding at a record-breaking center-of-mass energy of 13.7 TeV. In such conditions a single event can produce thousands of particles. The arrangement of multiple active pixel sensors offers the possibility of measuring several points of particle trajectories with high resolution. Reconstructing particle trajectories from those raw observations is an essential step in the interpretation of experimental data and it is a challenge in itself. The next section contains a very brief overview of the reconstruction process, better detailed in section 2.1.

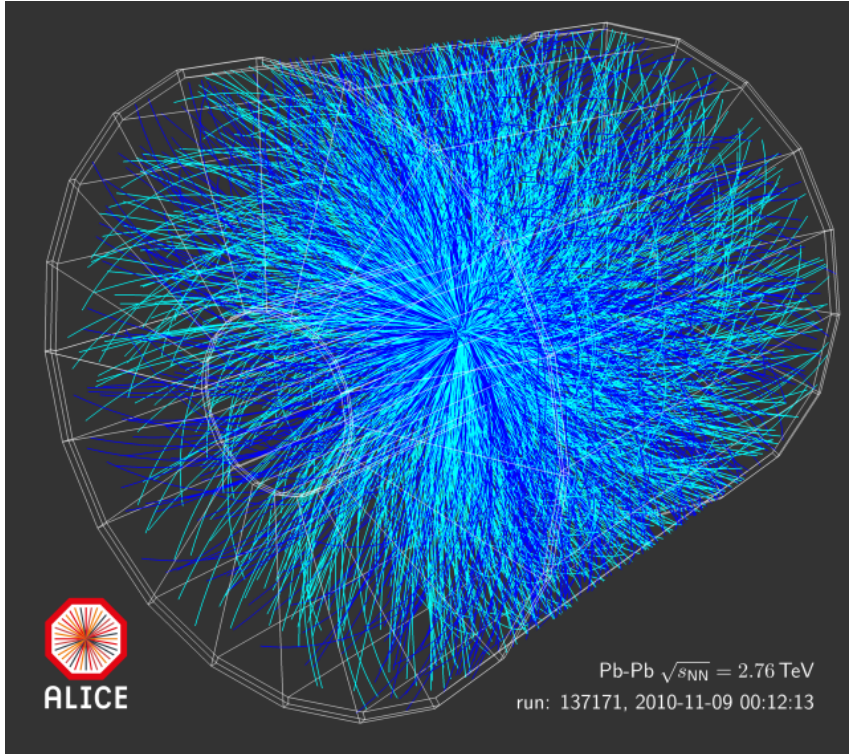


Figure 2: Display of reconstructed particles from a Pb-Pb collision at ALICE. The cylinder represents the *Time Project Chamber*. Original figure in CERN Document Server².

1.1.2 Particle-track reconstruction

Reconstruction is the process of estimating particle parameters, such as trajectory, charge and kinematic parameters from observations. Given a set of measurements, the main challenges are 1) to group observations originating from a given particle and 2) to obtain the best estimate for particle-parameters from this group of observations believed to be originated from the same particle. These two steps are usually referred to as *track finding* and *track fitting*, respectively.

Track fitting is the process of obtaining the best estimate for particle-track parameters from the set of observables. The least-squares methods is a well known and widely used method for this purpose. The Kalman Filter, a regressive fitting algorithm, is another common method and it is the baseline for track reconstruction in particle physics. In chapter 2, both methods are discussed.

Particle reconstruction is used extensively in all experiments of the Large Hadron Collider. Below one finds an introduction to the A Large Ion Collider Experiment (ALICE) and its upgrade, with emphasis given to particle tracking at forward geometries, the focus of the current work.

²<https://cds.cern.ch/record/2032743>

1.2 The A Large Ion Collider Experiment

ALICE is one of the four LHC main experiments. The detector weighs 10 thousand tons, have dimensions 26 m long, 16 m high and 16 m wide, sitting in a cavern 56 m bellow ground. It is designed to study the physics of strongly interacting matter, in particular the *Quark Gluon Plasma* (QGP). The experiment is optimized to observe particles produced by ultra-relativistic heavy ion collisions. For instance, ALICE is capable of measuring particles trajectories at high multiplicity with lower transverse *momentum* than the other experiments [16]. Results from ALICE shed light to some fundamental questions regarding matter formation, such as hadron formation and the generation of baryonic mass.

In order to carry out its scientific program ALICE relies on different sub-detectors, illustrated in figure 3. ALICE detectors are divided basically in the central barrel and the muon arm. The central part is within the L3 solenoid magnet, and contains the following detectors (from inner to outer layers): Inner Tracking System (ITS), Time-Projection Chamber (TPC), three Time-of-Flight (TOF) arrays, the High Momentum Particle Identification Detector (HMPID), a Transition Radiation Detector (TRD) and two electromagnetic calorimeters, Photon Spectrometer (PHOS) and Electromagnetic Calorimeter (EMCal). The muon arm is composed of the Muon Tracking Chambers (MCH), Muon Identifier (MID) and the Muon Forward Tracker (MFT). ALICE also counts on other smaller detectors: Zero Degree Calorimeter (ZDC), T0 and V0 [17].

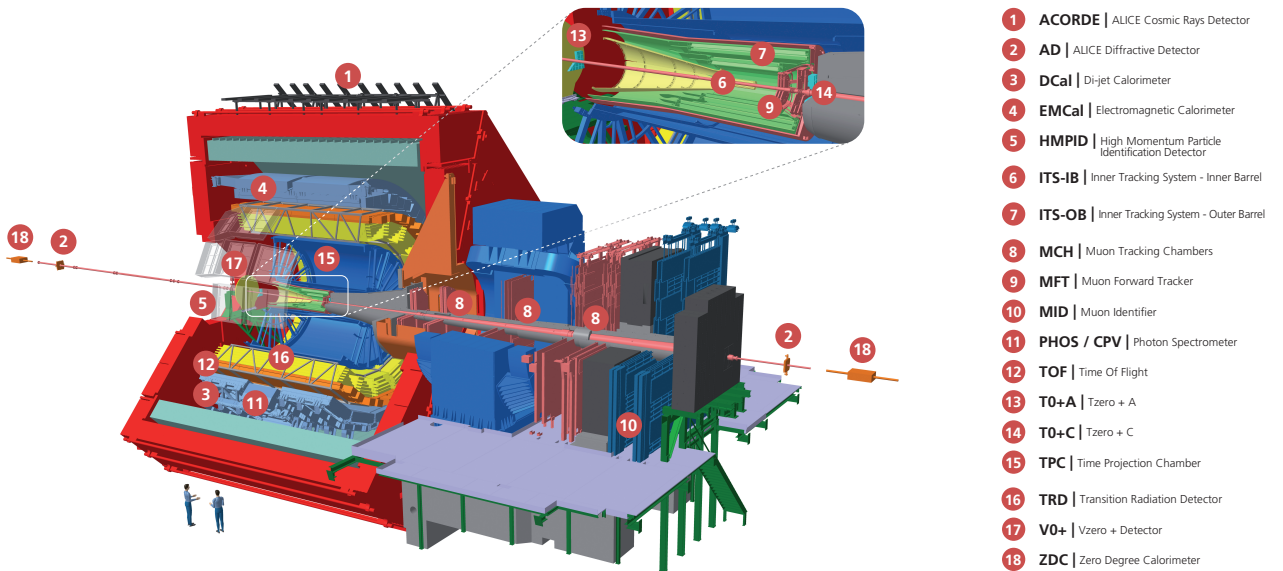


Figure 3: Illustration of ALICE and its sub-detectors, after RUN 3 upgrades. Original figure in CERN Document Server³.

In December 2018 LHC entered the Long Shutdown 2 (LS 2), a scheduled period when maintenance and upgrades are performed throughout the entire collider. The upgrades were executed in preparation for the third round of data taking (RUN 3) with a proposed increase in LHC integrated luminosity up to 300 fb^{-1} , but they also aim RUN 4 with the future High-Luminosity Large Hadron Collider (HL-LHC). To take benefit from the increased luminosity, ALICE has undergone a substantial upgrade of its detection systems, readout

³<https://cds.cern.ch/record/2263642>

electronics and software for data acquisition, processing and analysis. The new interaction rate for Pb beams will reach a value of about 50 kHz, translating into a raw data flow of more than 3 TB/s. This huge amount of data will be handled by the new ALICE online-offline system (ALICE O^2) [18], which will compress the data to a storage output of 0.1 TB/s [19]. The increase in data acquisition combined with the ALICE upgrades will provide detailed information about the primary vertex region, allowing a higher precision in vertex determination and, overall, a more detailed study about QGP and related phenomena. Essential for this, is the Muon Forward Tracker (MFT), a new detector installed at forward pseudo-rapidity region, conceived to improve vertexing resolution. An overview of all upgrades can be seen in [20] and the complete details can be found in the Letter of Intent for the ALICE upgrade [16]. In the next section the general ALICE physics program will be presented.

The Muon Forward Tracker (MFT) is designed to improve the vertex resolution by combining data acquired by it with data from other ALICE detectors. This will also allow improvement in present statistics, by increasing the signal/background ratio [21]. This project focuses on track reconstruction of the new MFT detector, described in more detail in section 1.2.3.

1.2.1 Scientific program of ALICE

The ALICE experiment studies the strongly interacting matter in QGP through heavy ions collisions. The upgrade will improve the signal to background ratio, allowing a better characterization of the QGP and deeper investigation of QCD topics, including the investigation of rare probes. Following the Letter of Intent of the ALICE upgrade [16] the main topics of study are:

- heavy flavour production: measurement of beauty and charm quarks production with high precision will enable studies of the heavy quarks thermalization and of the parton mass as well as colour-charge dependence of in-medium energy loss;
- production of quarkonia: detector upgrades will allow an improved measurement of J/ψ meson in p_t range $0 < p_t < 10$ GeV/c at high rapidity, in addition to complement ATLAS and CMS studies about Υ states;
- low-mass dileptons measurements trough e^+e^- channel: since electromagnetic radiation is produced at all stages of heavy-ion collisions, measurements of low-mass dileptons will give a better understanding on the evolution of matter created in these collisions. quantities such as the transport coefficients and the equation of state of the medium are potentially accessible with the disentanglement of early and late contributions of dilepton measurements;
- regarding jet measurements: several studies shall benefit from the upgrade such as: thermalization of fast quarks and gluons, heavy-flavour production (in jets), photon-jet correlations and jet quenching.
- heavy nuclear states: due to the excellent particle identification capabilities of ALICE, the experiment will be able to search for exotic objects, like the H dibaryon or states with multi-strange baryon, and its decays in an unique way.

In particular, the measurement of beauty and charm quarks at forward geometries requires the separation of prompt and non-prompt J/ψ . Prompt J/ψ are produced at the interaction point, while non-prompt J/ψ are those produced from beauty decays which have a longer decay length. The Muon Forward Tracker will have a fundamental role in this subject, as it will allow for distinguish primary vertices from secondary vertices near the interaction point.

1.2.2 The Muon Spectrometer

ALICE's Muon Spectrometer⁴ was the main apparatus in ALICE's forward region up to RUN 2 of the LHC, and it is specialized in heavy quarkonia detection - J/ψ , ψ' , Υ , Υ' , Υ'' - via decays in the muon channel. With a pseudo-rapidity coverage range of $2.5 < \eta < 4$, capability to detect the resonances of states down to $p_t = 0$ and invariant mass resolution of 70 MeV for J/ψ and 100 MeV for Υ it can measure all five resonance states. The invariant mass of dimuon pairs with a peak corresponding to J/ψ is shown in the spectrum in figure 4.

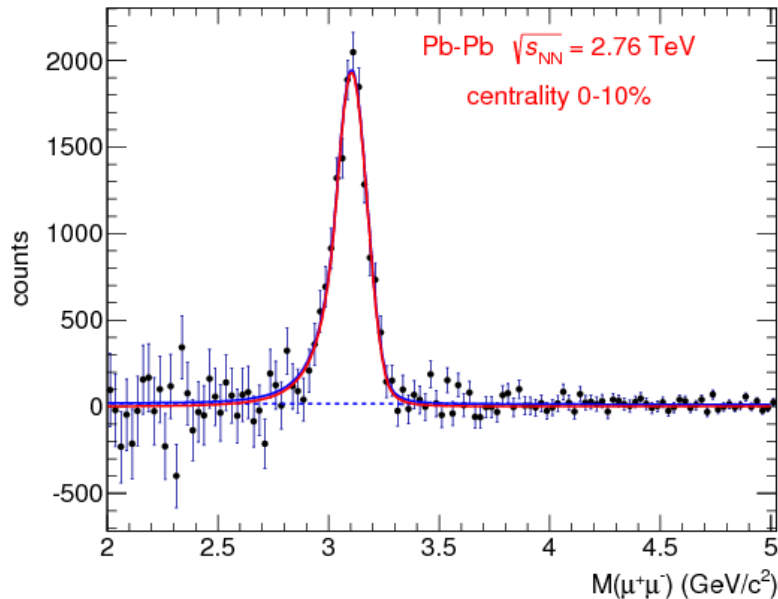


Figure 4: Invariant-mass distribution of $\mu^+ \mu^-$ pairs in 0-10% most central Pb-Pb collisions at center-of-mass energy of $\sqrt{s_{NN}} = 2.76\text{TeV}$ with a J/ψ peak at $\sim 3.1\text{ GeV}/c^2$. Originally in [22].

The four main components forming the Muon Spectrometer previous to the ALICE upgrade are listed bellow:

- absorber: a 4 m long carbon and concrete structure that suppresses all particles coming from the interaction point (and from subsequent decays) but muons. It's the main contributor of multiple scattering;

⁴<https://alice.cern/node/5532>

- tracking system: 10 cathode pad/strip chambers arranged in 5 stations of 2 chambers each. The radiation length is less than 3% per chamber in order to reduce the scattering of muons and reach a spatial resolution of 100 mm;
- trigger system: 4 planes of resistive plate chambers behind a muon filter provide the transverse *momentum* of each muon, with the objective of select heavy quark decays;
- dipole magnet: one of the biggest warm dipoles in the world, can generate a nominal magnetic field up to $B = 0.7$ T and field integral along beam axis of 3 Tm.

Figure 5 shows a schematic view of the Muon Spectrometer after the proposed upgrades, which includes the upgrade of the trigger system to the Muon Identifier (MID) [23, 24]. The Muon Forward Tracker is also represented.

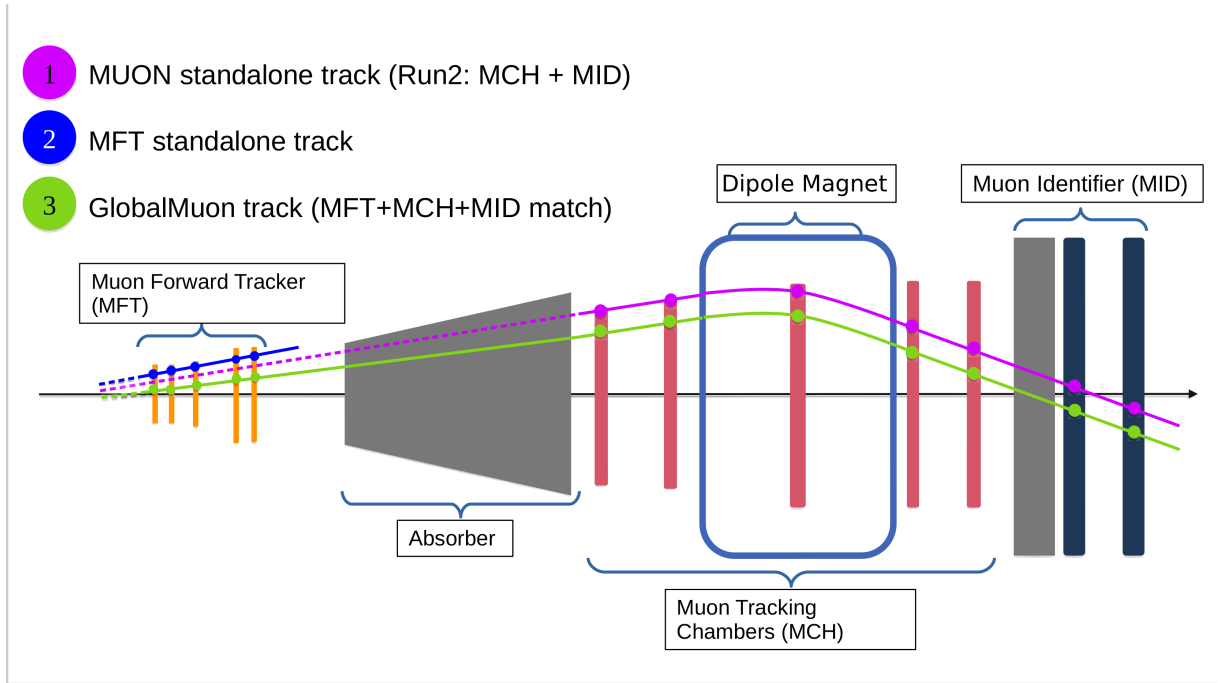


Figure 5: Schematic view of the Muon Spectrometer and the particle tracks as reconstructed by different detectors and their combinations.

Because of the material effects - mainly Multiple Coulomb Scattering and energy loss - the passage of muons through the absorber results in information loss about the particle origin. In practical terms we have:

- increased noise signal, due to difficulty in reject muons coming from semi-muonic decays of pions and kaon;
- it is not feasible to distinguish prompt J/ψ production from secondary productions;
- also impossible to distinguish muon production originating from open charm and from open beauty;
- limited mass resolution on observed resonances.

These limitations shall be overcome with information from the new Muon Forward Tracker, presented next.

1.2.3 The Muon Forward Tracker

The Muon Forward Tracker (MFT) is a new tracker detector of ALICE project installed during the Long Shutdown 2 (LS 2) as a part of the experiment upgrade for the third round of data taking (RUN 3). It was installed in a frontal geometry near the interaction point, complementing the Muon Spectrometer. MFT aims to increase the resolution on vertex determination of the particle trajectories observed by the Muon Tracking Chambers (MCH), allowing, for instance, to separate prompt and non-prompt components of J/ψ peaks like the one in figure 4.

The MFT is a conical telescope composed of 5 disks positioned along the beam axis at $z = 460, 493, 531, 687, 768$ mm from the nominal interaction point. Both faces of each disk are covered by MAPS sensors providing 10 detection planes (see figure 6). MFT covers the pseudo-rapidity range of $-3.6 < \eta < -2.45$, covering most of the muon spectrometer acceptance. The high granularity pixel detector gives a very small spatial resolution and the low material budget - $\langle x \rangle / X_0 \approx 0.4\%$ - prevents degradation of reconstructed track-parameter resolutions due to multiple scattering effects. It aims to complement the muon spectrometer, overcoming the existing limitation of lacking of information at the primary vertex region.

The MFT was installed between the interaction point and the absorber. Thus, particles hitting the MFT sensors will not have crossed the absorber, preventing information loss and allowing a more direct look at the particle origin. On the other hand, since the MFT is located before the filter, it receives signal of a huge amount of particles, which can generate significant background noise. In order to take advantage of MFT's location near the interaction point, it is necessary to match the reconstructed tracks at the MFT with the ones reconstructed by the muon spectrometer. The matching itself is challenging, as for one spectrometer track, there are many match candidates from the MFT. As a basic requirement for the match, a good and reliable track reconstruction at the MFT is essential. The combined reconstructed tracks will contain the unique information from each detector, allowing not only to improve existing measurements, like J/ψ , but to perform new studies as well.

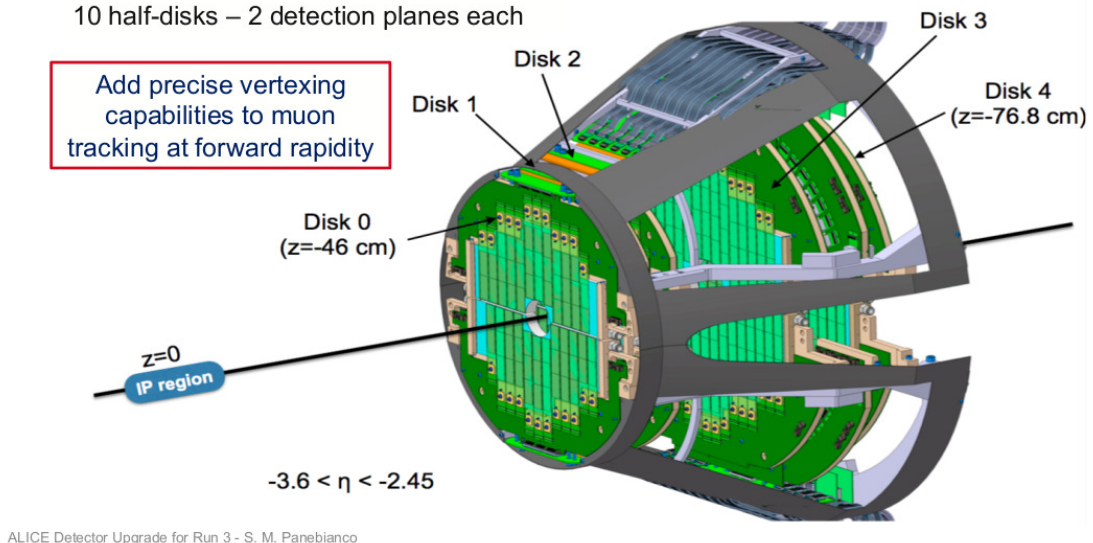


Figure 6: Schematic figure of MFT composition. MFT counts on 936 silicon pixel sensors on 240 ladders of 2 to 5 sensors each. Originally presented at the 40th International Conference on High Energy Physics.⁵

As a part of ALICE’s physics program, MFT will play an important role with respect to heavy flavor measurements and on separation of prompt and non-prompt dimuon pairs. In the MFT Letter of Intent [21], the following studies are listed:

- J/ψ and J/ψ' measurements: evaluation of the medium temperature and study of dissociation and regeneration mechanisms of charmonium;
- heavy flavour and charmonium elliptic flow measurements: pin down the medium equation of state and study about heavy quarks thermalization in-medium;
- extract of energy density of the medium, color charge and mass dependence of parton in-medium energy loss via measurements of heavy quark production (single muon channel) and J/ψ (b -hadrons decay);
- low-mass vector mesons measurement: investigation of the chiral nature of phase transitions.

1.3 Objectives of this project

This project aims at studying particle-track reconstruction at forward geometries and its application to the MFT detector at the ALICE experiment. The main elements of this study are 1) track reconstruction and 2) assessment of its quality.

Regarding particle-track reconstruction, this work aims at identifying a suitable coordinate system and track-models to describe particle trajectories at forward geometries and the

⁵https://indico.cern.ch/event/868940/contributions/3813685/attachments/2081068/3495497/Panebianco_ICHEP2020.pdf

corresponding implementation in C++ for integration into the ALICE O^2 computing system. The model must be adequate to evaluate the position resolution of the sensors and the interaction of charged particles with the detector material, in order to obtain accurate estimates of the track-parameter uncertainties. In what concerns the quality assessment of reconstructed track parameters, this work searches for appropriate quantities to qualify track reconstruction. It is also in the scope of this work, to compare different algorithms for track fitting, in order to define a consistent strategy for the track reconstruction assessment. Validation of the track reconstruction strategy can then be accomplished prior to real data taking using Monte Carlo simulations.

Objectively, we can summarize the goals as:

- identify suitable models for track trajectories and Multiple Coulomb Scattering effects;
- define a consistent strategy to assess the quality of reconstructed data and detector performance;
- compare reconstruction performance using different algorithms, comparing different track models and different fitting methods;
- evaluate effects on track reconstruction influenced by a) sensor resolution (measurement uncertainties) and b) detector material budget (which affects uncertainties propagation caused by the multiple scattering effect).

CHAPTER 2

THEORETICAL AND METHODOLOGICAL APPROACH

This chapter presents the theoretical concepts that serve as the basis for this project, as well as the methodology applied. Relevant concepts of track reconstruction, specially regarding track-fitting, are presented. This includes the mathematical representation of particle trajectories (track models), material effects on track-parameter resolution and fitting algorithms. The method and the tools created to obtain the results are presented, as well.

2.1 Particle-track reconstruction

Particle-track reconstruction, or *tracking* is the process of estimating the trajectory travelled by a particle. From this process one can retrieve important information about the particle, as its origin, charge and *momentum*, and thus about the system originating it. The main steps of the tracking are *track finding* and *track fitting*. The goal of track finding is to group the signals from the sensors (hits), creating a track candidate. Several different techniques can be used in track finding, for example Conformal Transformation, Hough Transform, Cellular Automaton and Machine Learning. For more information on these and other methods for track finding one can refer to [12, chapter 5]. The MFT currently uses two methods for track-finding, executed in two consecutive steps. The first method is called Linear Track Finder and is suitable for high-momentum tracks. The second method is based on a Cellular Automaton and it is suitable for tracks that deviates from linear trajectories, either by means of track-curvature due magnetic field effects or due to scattering events in the detector material. Appendix A presents an overview of MFT track finding. Track Fitting aims at estimating the best parameters and covariance matrix of a track candidate, considering a mathematical model for the particle trajectories and taking into account the detector's specific features. We can find several approaches for the track-fitting process, for example: the extended Kalman filter, regression with breakpoints and several methods based on the least-squares principle. For a overview on these and other techniques see [12, chapter 6]. MFT track fitting is performed with Kalman Filter, which will be discussed in section 2.1.3.2.

In the next subsections, some important topics with respect to track reconstruction will be discussed. Track-models will be the first topic addressed, followed by track-parameter resolution and factors that can affect it. Last, the estimation of the track parameters and of the covariance matrix using the Kalman Filter is presented.

2.1.1 Track models

The track model is a mathematical representation of the path of a charged particle and it is composed by the propagator of track parameters and its Jacobian, responsible for the covariance matrix propagation. A model can be obtained by solving the equations of motion of the system and the solution will depend on the coordinate system, conveniently chosen in respect to the detector's layout. If the equations of motion cannot be solved analytically, numerical integration is necessary. An appropriate choice of the model is important in selecting the fitting method, since the fitting must be able to handle the existing (or not) track curvature. If the chosen track model is a bad representation of the particle trajectory, the reconstruction process will produce poor results.

Usually, the choice of the track model depends basically on the magnetic field. With no field present a linear model shall be appropriate, since the particles will move in a straight line. In the case of a homogeneous magnetic field, as it is the case for the central region of the ALICE experiment, charged particles will follow a helical trajectory, since their motion is determined by the Lorentz force. Still, there are cases where even within a field, the particle moves in an almost straight line. In such cases the model may be simplified, by expanding the equations of motion to a second order or even first order approximation. In order to elaborate on the track models used in this work, the MFT coordinate system will be presented first.

MFT coordinate system

Typically, coordinate systems used in the tracker detectors are formed by two quantities related to position, two related to directions and one to *momentum* and charge. From the *momentum*, one can obtain the track curvature (see section 2.1.2), whose sign will be given by the particle charge q . Although the charge itself could be an individual parameter, it is easily incorporated by the *momentum*, representing the *charged momentum*. The *momentum* information can still be written in the form of the transverse *momentum* p_t . The coordinate system used for MFT track reconstruction consists of the following quantities:

- x and y Cartesian coordinates of the track trajectory;
- ϕ angle: direction of the transverse *momentum* p_t on the xy-plane;
- $\tan \lambda$, where λ is the track dip angle and it is complementary to the polar angle θ ;
- q/p_t : inverse charged transverse *momentum*, where q corresponds to the particle charge.

Here $p_t = \sqrt{p_x^2 + p_y^2}$ is the transverse *momentum*, where p_x and p_y are the x and y components of a particle total *momentum* \vec{p} . All these quantities are illustrated in figure 7. The following equations relate the Cartesian and MFT coordinate systems:

$$p = \frac{p_t}{\cos \lambda} = \frac{1}{|q/p_t| \cos \lambda}^1, \quad (2.1)$$

$$p_t = \sqrt{p_x^2 + p_y^2}, \quad (2.2)$$

$$\tan \phi = \frac{p_y}{p_x}, \quad (2.3)$$

$$\tan \lambda = \frac{p_z}{p_t} \quad (2.4)$$

A more detailed discussion of these and other useful relations, as well as the conversion between MFT and MCH coordinate systems, are presented in appendix B.

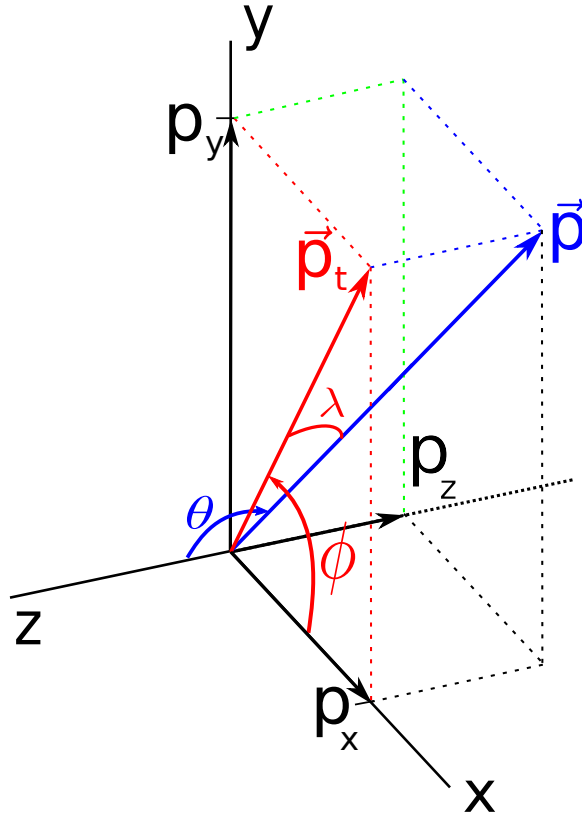


Figure 7: Representation of the MFT coordinate system. The total *momentum* \vec{p} and its x , y and z and transverse components are also shown. Solid black lines indicate axes positive directions. λ is negative for tracks moving towards the MFT.

A state vector \mathbf{s} of a charged particle written in terms of MFT coordinate system reads as:

$$\mathbf{s} = (x, y, \phi, \tan \lambda, q/p_t). \quad (2.5)$$

¹Here we substitute p_t by the inverse charged transverse *momentum* q/p_t mentioned before. To maintain the equality it is necessary to take the absolute value of q/p_t , since q takes on values of ± 1 , accordingly to the track curvature.

Helix track model:

Ideally one should use a Helix track model in describing charged particle trajectories moving on an uniform magnetic field. In this case, the general equation of the trajectory can be written as a function of the path length s , as [25, 26]:

$$\mathbf{M} = \mathbf{M}_0 + \frac{\gamma}{Q}(\delta - \sin \delta) \cdot \mathbf{H} + \frac{\sin \delta}{Q} \cdot \mathbf{T}_0 + \frac{\alpha}{Q}(1 - \cos \delta) \cdot \mathbf{N}_0 \quad (2.6)$$

where \mathbf{M} is the position vector, $\mathbf{H} = \mathbf{B}/|\mathbf{B}|$ is the normalized magnetic field, $\mathbf{T} = \mathbf{p}/|\mathbf{p}|$ is the unit vector tangent to the track, $\alpha = |\mathbf{H} \times \mathbf{T}|$, $\mathbf{N} = (\mathbf{H} \times \mathbf{T})/\alpha$ is the normal vector to the track, $\gamma = \mathbf{H} \cdot \mathbf{T}$, $Q = -q|\mathbf{B}|/|\mathbf{p}|$ and $\delta = Q \cdot s$. The quantities with subscript 0 are defined at a reference point.

To obtain the track model we must know how the state vector (2.5) evolves. We can find x and y by writing (2.6) in the MFT coordinate system, where $\mathbf{B} = (0, 0, B_z)^2$:

$$\mathbf{M} = \begin{bmatrix} x \\ y \\ z \end{bmatrix} = \begin{bmatrix} x_0 - \frac{H_z}{(q/p_{t0})k} \sin(\phi_0) \cos\left(\frac{(q/p_{t0})\Delta z k}{\tan \lambda_0}\right) + \frac{H_z}{(q/p_{t0})k} \sin(\phi_0) + \frac{\cos(\phi_0)}{(q/p_{t0})k} \sin\left(\frac{(q/p_{t0})\Delta z k}{\tan \lambda_0}\right) \\ y_0 + \frac{H_z}{(q/p_{t0})k} \cos(\phi_0) \cos\left(\frac{(q/p_{t0})\Delta z k}{\tan \lambda_0}\right) - \frac{H_z}{(q/p_{t0})k} \cos(\phi_0) + \frac{\cos(\phi_0)}{(q/p_{t0})k} \sin\left(\frac{(q/p_{t0})\Delta z k}{\tan \lambda_0}\right) \\ z_0 + \Delta z \end{bmatrix}, \quad (2.7)$$

where $k = 0.3|B_z|$ (the constant factor 0.3 is originated from unit conversion). ϕ rotates accordingly to the helical movement (see chapter 3.3.1 of [25]) and its variation $\Delta\phi$ will be:

$$\Delta\phi = -\frac{(q/p_{t0})\Delta z}{\tan \lambda_0} H_z. \quad (2.8)$$

Along the particle trajectory, $\tan \lambda$ and q/p_t are constants of motion. p_t is the component of the total *momentum* p in the xy -plane, thus $\tan \lambda$ does not change. Since there is no radial force in the MFT system, p_t also does not change. Then, the helix propagator for a particle track in MFT is:

$$\begin{bmatrix} x \\ y \\ \phi \\ \tan \lambda \\ q/p_t \end{bmatrix} = \begin{bmatrix} x_0 - \frac{H_z}{(q/p_{t0})k} \sin(\phi_0) \cos\left(\frac{(q/p_{t0})\Delta z k}{\tan \lambda_0}\right) + \frac{H_z}{(q/p_{t0})k} \sin(\phi_0) + \frac{\cos(\phi_0)}{(q/p_{t0})k} \sin\left(\frac{(q/p_{t0})\Delta z k}{\tan \lambda_0}\right) \\ y_0 + \frac{H_z}{(q/p_{t0})k} \cos(\phi_0) \cos\left(\frac{(q/p_{t0})\Delta z k}{\tan \lambda_0}\right) - \frac{H_z}{(q/p_{t0})k} \cos(\phi_0) + \frac{\sin(\phi_0)}{(q/p_{t0})k} \sin\left(\frac{(q/p_{t0})\Delta z k}{\tan \lambda_0}\right) \\ \phi_0 - \frac{(q/p_{t0})\Delta z k}{\tan \lambda_0} H_z \\ \tan \lambda_0 \\ (q/p_{t0}) \end{bmatrix}. \quad (2.9)$$

The associated Jacobian responsible for the uncertainty propagation is given by the

²MFT's position within the solenoid magnet allows for an uniform field approximation, where only the z component exists.

first-order partial derivatives of the propagator in respect to the track parameters $\mathbf{p}_0 = \{x_0, y_0, \phi_0, \tan \lambda_0, q/p_{t0}\}$:

$$\mathbf{J} = \begin{bmatrix} \frac{\partial x}{\partial x_0} & \frac{\partial x}{\partial y_0} & \frac{\partial x}{\partial \phi_0} & \frac{\partial x}{\partial (\tan \lambda_0)} & \frac{\partial x}{\partial (q/p_{t0})} \\ \frac{\partial y}{\partial x_0} & \frac{\partial y}{\partial y_0} & \frac{\partial y}{\partial \phi_0} & \frac{\partial y}{\partial (\tan \lambda_0)} & \frac{\partial y}{\partial (q/p_{t0})} \\ \frac{\partial \phi}{\partial x_0} & \frac{\partial \phi}{\partial y_0} & \frac{\partial \phi}{\partial \phi_0} & \frac{\partial \phi}{\partial (\tan \lambda_0)} & \frac{\partial \phi}{\partial (q/p_{t0})} \\ \frac{\partial \tan \lambda}{\partial x_0} & \frac{\partial \tan \lambda}{\partial y_0} & \frac{\partial \tan \lambda}{\partial \phi_0} & \frac{\partial \tan \lambda}{\partial (\tan \lambda_0)} & \frac{\partial \tan \lambda}{\partial (q/p_{t0})} \\ \frac{\partial (q/p_t)}{\partial x_0} & \frac{\partial (q/p_t)}{\partial y_0} & \frac{\partial (q/p_t)}{\partial \phi_0} & \frac{\partial (q/p_t)}{\partial (\tan \lambda_0)} & \frac{\partial (q/p_t)}{\partial (q/p_{t0})} \end{bmatrix}. \quad (2.10)$$

Then, for the helix model the Jacobian is:

$$\begin{bmatrix}
1 & 0 & -\frac{H_z A}{(q/p_0)k} + \frac{H_z \cos(\phi_0)}{(q/p_0)k} - \frac{B}{(q/p_0)k} & -\frac{H_z E B}{\tan\lambda_0} - \frac{E A}{\tan\lambda_0} \\
0 & 1 & -\frac{H_z C}{(q/p_0)k} + \frac{H_z \sin(\phi_0)}{(q/p_0)k} + \frac{D}{(q/p_0)k} & -\frac{H_z E D}{\tan\lambda_0} - \frac{E C}{\tan\lambda_0} \\
0 & 0 & 1 & \frac{\theta}{\tan\lambda_0} H_z \\
0 & 0 & 0 & 0 \\
0 & 0 & 1 & 0 \\
0 & 0 & 0 & 1
\end{bmatrix}
\left[\begin{array}{l}
\frac{H_z C}{(q/p_0)^2 k} - \frac{H_z \sin(\phi_0)}{(q/p_0)^2 k} - \frac{D}{(q/p_0)^2 k} + \frac{H_z E B}{(q/p_0)} + \frac{E A}{(q/p_0)} \\
-\frac{H_z A}{(q/p_0)^2 k} + \frac{H_z \cos(\phi_0)}{(q/p_0)^2 k} - \frac{B}{(q/p_0)^2 k} - \frac{H_z E D}{(q/p_0)} + \frac{E C}{(q/p_0)} \\
-\frac{H_z A}{(q/p_0)^2 k} + \frac{H_z \cos(\phi_0)}{(q/p_0)^2 k} - \frac{B}{(q/p_0)^2 k} - \frac{H_z E D}{(q/p_0)} + \frac{E C}{(q/p_0)} \\
-H_z E k
\end{array} \right]$$
(2.11)

where:

- $\theta = \frac{(q/p_{t0})\Delta z k}{\tan \lambda_0}$
- $A = \cos(\phi_0) \cos(\theta)$
- $B = \sin(\phi_0) \sin(\theta)$
- $C = \sin(\phi_0) \cos(\theta)$
- $D = \cos(\phi_0) \sin(\theta)$
- $E = \frac{\Delta z}{\tan \lambda_0}$.

Quadratic track model (second order approximation):

As the effects of the fields within the MFT are weak [21, 27], approximated track models may be used in describing the particle trajectory. Expanding the helix equations into a Taylor's series, it is possible to approximate the track model to a parabolic function by taking the values up to the second order of the expansion. The propagator (2.9) in this quadratic approximation becomes:

$$\begin{bmatrix} x \\ y \\ \phi \\ \tan \lambda \\ q/p_t \end{bmatrix} = \begin{bmatrix} x_0 + \frac{\Delta z}{\tan \lambda_0} \cos(\phi_0) + \frac{(q/p_{t0})H_z \Delta z^2 k}{2 \tan \lambda_0^2} \sin(\phi_0) \\ y_0 + \frac{\Delta z}{\tan \lambda_0} \sin(\phi_0) - \frac{(q/p_{t0})H_z \Delta z^2 k}{2 \tan \lambda_0^2} \cos(\phi_0) \\ \phi_0 - \frac{(q/p_{t0})\Delta z k}{\tan \lambda_0} H_z \\ \tan \lambda_0 \\ (q/p_{t0}) \end{bmatrix} \quad (2.12)$$

The associated Jacobian, obtained the same way as in the helix model, is:

$$\begin{bmatrix} 1 & 0 & -\frac{\Delta z \sin(\phi_0)}{\tan \lambda_0} + \frac{(q/p_{t0})H_z \Delta z^2 k \cos(\phi_0)}{2 \tan \lambda_0^2} & -\frac{\Delta z \cos(\phi_0)}{\tan \lambda_0^2} - \frac{(q/p_{t0})H_z \Delta z^2 k \sin(\phi_0)}{\tan \lambda_0^3} & \frac{H_z \Delta z^2 k \sin(\phi_0)}{2 \tan \lambda_0^2} \\ 0 & 1 & \frac{\Delta z \cos(\phi_0)}{\tan \lambda_0} + \frac{(q/p_{t0})H_z \Delta z^2 k \sin(\phi_0)}{2 \tan \lambda_0^2} & -\frac{\Delta z \sin(\phi_0)}{\tan \lambda_0^2} + \frac{(q/p_{t0})H_z \Delta z^2 k \cos(\phi_0)}{\tan \lambda_0^3} & \frac{H_z \Delta z^2 k \cos(\phi_0)}{2 \tan \lambda_0^2} \\ 0 & 0 & 1 & \frac{(q/p_{t0})H_z \Delta z k}{\tan \lambda_0^2} & -\frac{H_z \Delta z k}{\tan \lambda_0} \\ 0 & 0 & 0 & 1 & 0 \\ 0 & 0 & 0 & 0 & 1 \end{bmatrix} \quad (2.13)$$

Linear track model (first order approximation):

In some cases, specially at high p_t , particles follow almost straight trajectories, where the linear approximation may yield good results. However, this does not allow evaluation of the inverse charged *momentum*, since the particle charge is determined by the track curvature. This model can also be used in the absence of magnetic fields. The linear propagator is given by:

$$\begin{bmatrix} x \\ y \\ \phi \\ \tan\lambda \\ q/p_t \end{bmatrix} = \begin{bmatrix} x_0 + \frac{\Delta z \cos(\phi_0)}{\tan\lambda_0} \\ y_0 + \frac{\Delta z \sin(\phi_0)}{\tan\lambda_0} \\ \phi_0 \\ \tan\lambda_0 \\ (q/p_{t0}) \end{bmatrix}, \quad (2.14)$$

and the corresponding Jacobian is given by:

$$\begin{bmatrix} 1 & 0 & -\frac{\Delta z \sin(\phi_0)}{\tan\lambda_0} & -\frac{\Delta z \cos(\phi_0)}{\tan\lambda_0^2} & 0 \\ 0 & 1 & \frac{\Delta z \cos(\phi_0)}{\tan\lambda_0} & -\frac{\Delta z \sin(\phi_0)}{\tan\lambda_0^2} & 0 \\ 0 & 0 & 1 & 0 & 0 \\ 0 & 0 & 0 & 1 & 0 \\ 0 & 0 & 0 & 0 & 1 \end{bmatrix} \quad (2.15)$$

Near the MFT, where the magnetic field is considered homogeneous and the particles are not very sensitive to its effects due their high *momentum*, one expects that the quadratic track model could describe the particle tracks as well as the helix track model. This would allow for a simpler description and calculations, specially code-wise. Comparisons between track reconstruction based on the helix model and its approximations are shown in section 3.3.1.1.

2.1.1.1 Multiple Coulomb Scattering effects

Multiple Coulomb Scattering (MCS) is responsible to deviate a particle from its ideal trajectory due to matter interaction. The denser the material and the longer is the material length, the more a particle can be scattered. In ALICE's MUON arm, particle tracks are subject to outstanding material effects due to the particle passage through the absorber (a 4 m carbon and concrete particle filter). Multiple scattering effects also depends on the *radiation length* X_0 . The radiation length of a material is the mean length that a charged particle has to travel inside this material to have its energy reduced by a factor of $1/e$, due to radiation loss (bremsstrahlung). If the thickness of a material is expressed in terms of the radiation length X_0 , then the radiation loss can be expressed independently of the material.

Multiple scattering effects are quantified by a scattering angle θ_{plane} , (shown in figure 8³) and it is applied in track reconstruction as a part of the covariance matrix. To compute this contribution in covariance matrices, we must then have the variance of θ_{plane} . For thin scatterers, the variance $\sigma_{\theta_{plane}}$ for one layer is given by [15, 28]:

$$\sigma_{\theta_{plane}} = \frac{0.0136 \text{GeV}/c}{\beta p} \sqrt{\frac{x}{X_0}} \left[1 + 0.038 \ln \left(\frac{x}{X_0} \right) \right], \quad (2.16)$$

where β and p are the velocity and *momentum*, respectively, and x/X_0 is the thickness of one

³The quantities S_{plane} , Ψ_{plane} and y_{plane} , also shown in figure 8, are sometimes used to describe MCS, but are not used for this purpose here.

detector plane in units of radiation length.

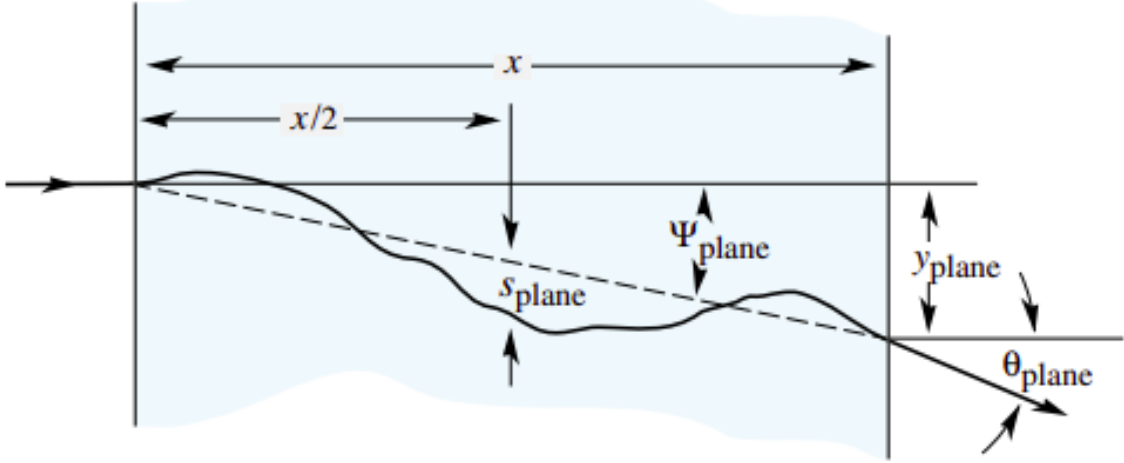


Figure 8: Illustration of the multiple scattering effect and the quantities used to describe it [15].

The actual implementation of the multiple scattering effect depends on the fitter algorithm. In global least-squares methods, as will be seen in section 2.1.3.1, the influence of all detection layers are evaluated in a same matrix. On the other hand, for the Kalman Filter (section 2.1.3.2), the effects are accounted for in each step of the algorithm.

2.1.2 Track-parameter and uncertainties

This section addresses the physical principles of tracking parameter measurement and the corresponding uncertainties. Once the physical and geometrical basis of track-parameter measurement are presented, the next section follows with the computational methods applied to track reconstruction.

Track-parameter resolutions are key indicators of detector and reconstruction performance. Resolutions are usually represented as the standard deviations of the distribution of residuals, i.e., the differences between the true and the estimated value of the parameter. Parameter resolutions can be affected by several factors, from the design of the experiment and validity of the track model to the implementation of the reconstruction algorithms. A covariance matrix contains information about track parameter uncertainties and their relations. This matrix also plays a fundamental role when of the track fitting process, working as weights to measurements. In summary, a covariance matrix indicates how reliable a measurement is.

Principles of track parameter measurements

The only direct measurements of particle-track parameters in MFT are the x and y positions at the specific z positions of the MFT detection planes. The other track-parameters must be inferred from them. The angular parameters, ϕ_0 and $\tan\lambda_0$ can be obtained from two clusters

by:

$$\phi_0 = \arctan\left(\frac{\Delta y}{\Delta x}\right) - \mathcal{O}\left(\tan\lambda_0, \frac{q}{p_{t_0}}\right), \quad (2.17)$$

$$\tan\lambda_0 = \frac{\Delta z}{\sqrt{(\Delta x)^2 + (\Delta y)^2}}, \quad (2.18)$$

where Δx , Δy and Δz are the Cartesian distances between two measurements. These quantities are illustrated in figure 9a. The second term of ϕ_0 is the correction due the propagation and is the same as in equation (2.9). $\tan\lambda$ is approximately constant and does not need corrections from track propagation⁴. As both ϕ_0 and $\tan\lambda_0$ depends on Δx and Δy , the angular parameters are also subjected to the resolution of the sensor.

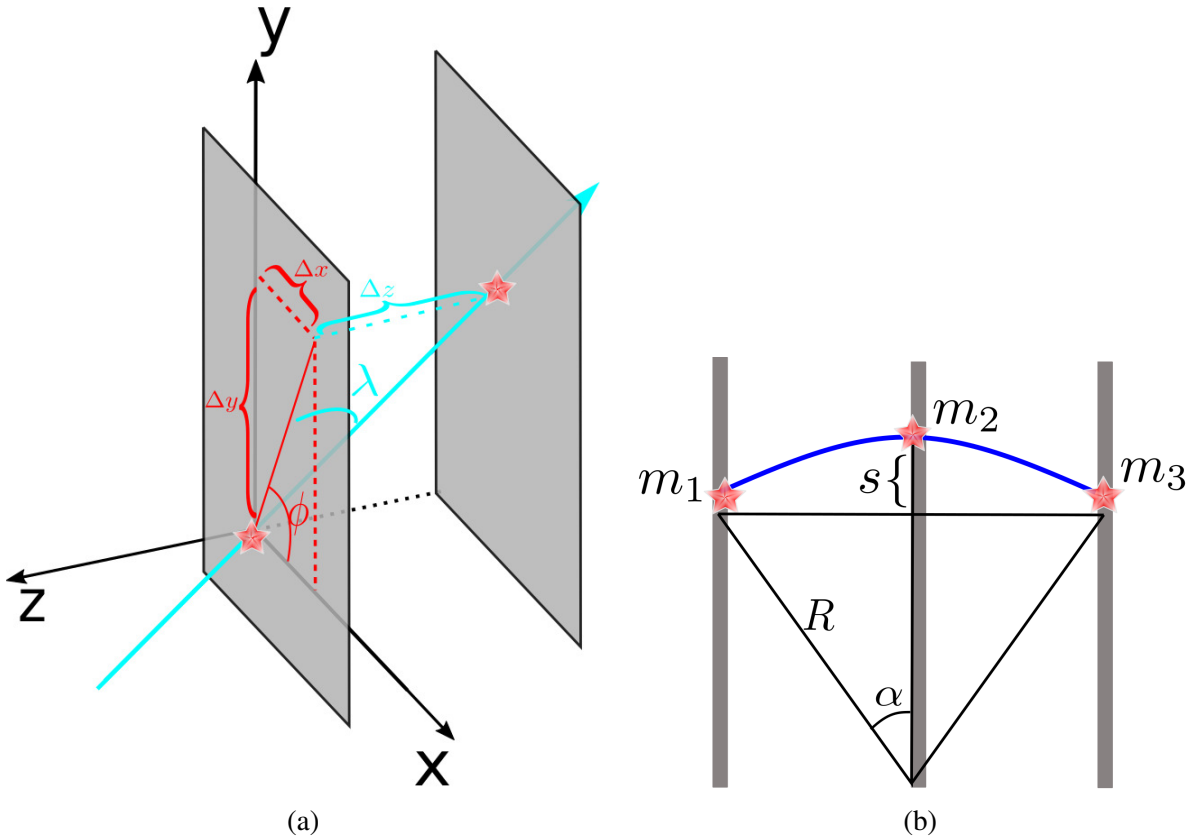


Figure 9: Illustration of geometrical concepts used to estimate MFT track-parameters. (a): from two measurements the angular parameters ϕ and $\tan\lambda$ can be calculated, in addition to the position measurements. (b): calculation of q/p_t need at least three measurements, in order to find the track curvature R ; s is the sagitta formed form the three measurements and α the angle between the measurements m_1 and m_2 .

The last parameter, q/p_{t_0} , needs at least three measurements, since it is based on the track curvature. From the Lorentz Force, $\mathbf{F}_L = q \cdot \mathbf{v} \times \mathbf{B}$, and Centripetal Force, $\mathbf{F}_C = m \cdot \mathbf{v}^2/R$, one can find the relation:

$$p_t = 0.3BR \text{ GeV/c}, \quad (2.19)$$

⁴At high p_t $\tan\lambda$ is approximately constant and this was seen to be valid for MFT reconstruction, but must be taken cautiously if applied to another detector layout.

where R is the radius of the circle associated to the motion caused by the Lorentz Force. The constant 0.3 derives from unit conversion. The radius can then be found using the sagitta s (which is the distance from the center of an arc to the center of its base) shown in figure 9b.

Figure 9b illustrates the trajectory of a particle with three measurements m_1, m_2 and m_3 , the minimum necessary to estimate q/p_t . The trajectory is an arc of radius R and length L . The equations bellow relate the sagitta s (which can be formed by at least 3 measurements) with the radius R , when $s \ll L$, and also the p_t error δ_{p_t} with the measurement error δm , for when the size of s is approximately the same as δm :

$$s \approx \frac{R\alpha^2}{2} = \frac{L^2}{8R} \quad (2.20)$$

$$\delta s = \frac{L^2}{8R^2} \delta R \quad (2.21)$$

$$\frac{\delta p_t}{p_t} = \frac{\delta R}{R}, \quad \delta s \sim \delta m \quad (2.22)$$

$$\frac{\delta p_t}{p_t} \simeq \frac{8p_t}{0.3BL^2} \delta m \quad (2.23)$$

Equation (2.23) relates the error on the transverse *momentum* estimation with the measurement error, that is, it shows the dependence of p_t regarding the sensor resolution. The practical implementation to find the trajectory curvature in MFT reconstruction follows the “Fast Circle Fit” (FCF) method in [29]. Briefly, the FCF uses a conformal transformation to map a curve path into a straight line; then, by using a linear regression the parameters of interest can be found.

Uncertainties and detector resolution

The position of a cluster is the only direct observable of the track-parameters at each measurement, nevertheless, the position uncertainties are incorporated into the covariance matrix. At high *momentum*, sagittas are very small, since particle trajectories are close to straight lines. Also, in this kinematic regime multiple scattering effects are weaker than at low *momentum*, therefore, for high p_t particle-tracks, the *momentum* resolution is constrained by the sensor resolution.

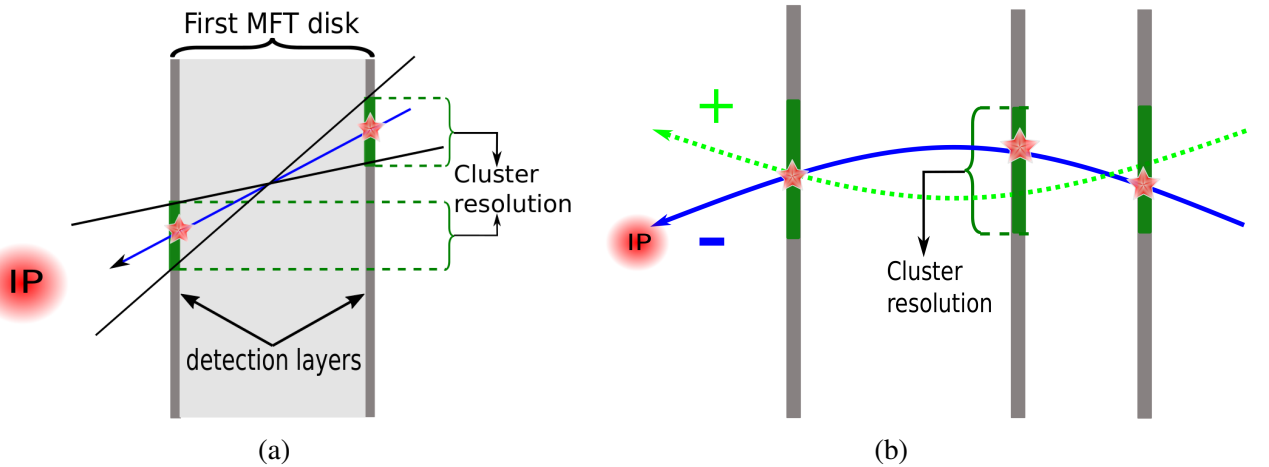


Figure 10: Illustration of cluster resolutions and the propagation effects on vertex estimation. “IP” stands for “interaction point”. This figure illustrates the effects of resolutions, not reproducing the actual scale of experiments nor the particle direction.

Figure 10 illustrates how the uncertainty of measurements can affect vertexing and q/p_t resolutions. Figure 10a depicts how the uncertainties of two clusters form a conical volume that contains a straight track. In figure 10b the uncertainty on the estimation of q/p_t may even give a wrong sign to the curvature, if particle charge is mismatch, and can have huge impact in propagating the track to the vertex region.

In principle one could think that the sensor resolution would be defined by the dimensions of a single pixel. Nevertheless, more than one pixel is usually activated by the passage of a single charged particle through a MAPS sensor due to charge diffusion. In such cases the particle position is calculated using a combined resolution of the pixels, which allows a more precise measurement. There can be several topologies of clusters, each topology with a particular resolution. An illustration of some types of topology can be seen in figure 11. This information can be used in track reconstruction via a *cluster dictionary*, which organizes cluster patterns and their associated errors for each coordinate.

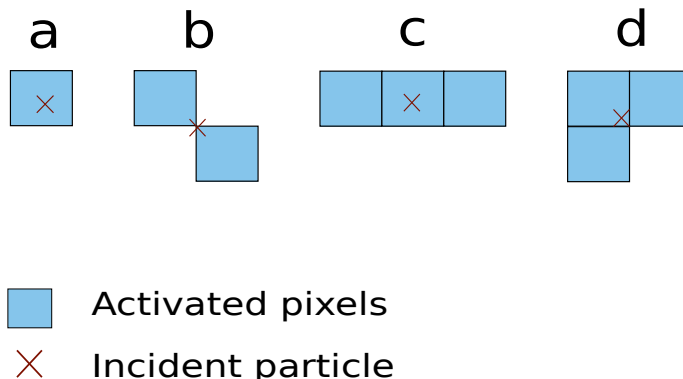


Figure 11: Examples of possible cluster topologies generated by a particle hit. (a) one pixel activated; (b) two pixels activated; (c) and (d) three pixels activated. Adapted from [30].

Having the physical principles of particle track reconstruction and the corresponding track-parameters resolutions presented, we now focus on *track fitting*, the computational

methods used to determine the particle-track parameters and their covariance matrix.

2.1.3 Track fitting

In the *track fitting* step the track parameters and the associated covariance matrix are adjusted accordingly to the measured clusters, aiming for the most accurate description of the particle trajectory. There are several methods able to achieve this goal. In this section, we present two of them: the traditional χ^2 -minimization and the Kalman Filter, which is often used in particle physics.

2.1.3.1 χ^2 -minimization

Least-square methods are very common and widely used techniques for track fitting, which search the optimal parameters values by minimizing the sum of squares of the residuals r_k

$$S = \sum_{k=1}^N r_k^2, \quad r_k = \mathbf{m}_k - \mathbf{f}(\mathbf{x}_k, \mathbf{p}). \quad (2.24)$$

N is the number of measurement points (detection layers). The residuals are the difference between the observed variables \mathbf{m} and its estimated value through the function $\mathbf{f}(\mathbf{x}, \mathbf{p})$ (with independent variable \mathbf{x} and adjustable parameters \mathbf{p}). For instance, the function can be the track propagators discussed in section 2.1.1. Based on the least-square method we can highlight the χ^2 minimization, which aims to minimize the χ^2 function:

$$\chi^2 = \sum_{k=1}^N \frac{r_k^2}{\sigma_k}, \quad (2.25)$$

where σ_k represents measurements uncertainties. It's a rather straightforward process, in which the algorithm will change the values of the parameters \mathbf{p} trying to minimize χ^2 . Figure 12 shows a comparison of two models for the same data set, where we can see how a lower value for the χ^2 provides better results. The capabilities of the fitter will greatly depend on its initial configuration, mainly the step used in the parameters variation and the error tolerance (on the function value at the minimum). A step too large may not have enough sensibility to reach the global χ^2 minimum, since it would bounce between edge values. On the other hand, if the step is too small, the fitting can end in a local minimum, or, if not enough number of interactions occur, calculations can stop before reaching a minimum.

Equation 2.25 can also be written in matrix form:

$$\chi^2 = \sum_{i=1}^M (\mathbf{y}_i - \mathbf{f}_i)^T \mathbf{W}_i (\mathbf{y}_i - \mathbf{f}_i) \quad (2.26)$$

where M is the dimension of vector \mathbf{m}_k , i.e., the number of observable parameters in one detection layer; $\mathbf{y} = (y_0, y_1, \dots, y_N)$ is a measured parameter in the N detector planes and \mathbf{W} is a weight matrix related to the covariance matrix of the system.

So that the variances are minimized, the weight matrix assumes the form: $\mathbf{W} = C_y^{-1}$, where C_y is the covariance matrix for y . The covariance matrix takes contributions from the sensor error

and multiple scattering effects, as given by [28]:

$$(C_y)_{mn} = \sigma_n^2 \delta_{mn} + \sum_{j=0}^{\text{Min}[m,n]-1} \sigma_{\alpha_j}^2 (z_m - z_j)(z_n - z_j), \quad (2.27)$$

where σ_n^2 represents the variance related to the sensor resolution and $\sigma_{\alpha_j}^2$ the variance due a scattering angle α at layer j ⁵. The sub-indices m and n go from 0 to N (number of measurements).

In this work, the χ^2 -minimization was applied with the use of the MINUIT fitter⁶. MINUIT is numerical minimization library, which takes as inputs from the user parameters to be adjusted and a function to be minimized, that in our case shall be equation (2.26). MINUIT was originally written in FORTRAN by Fred James, but it was ported to C++ and now integrates the ROOT Data Analysis Framework. At the end of the minimization, the routine returns the estimated values for the track parameters at the first MFT layer and the associated covariance matrix.

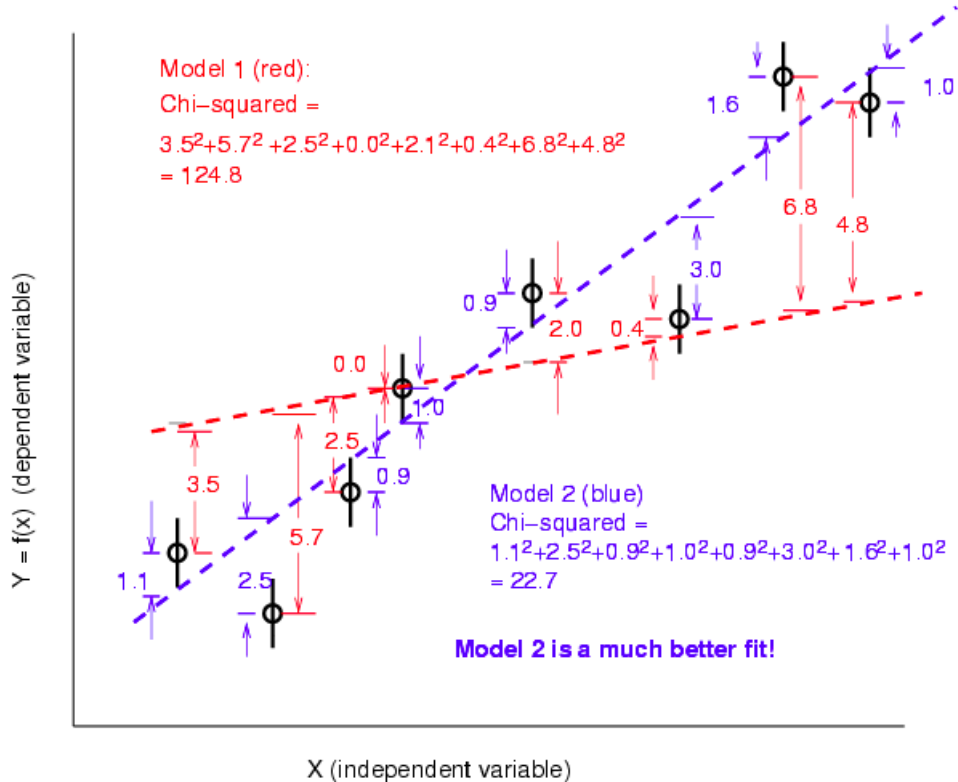


Figure 12: Example of fitting using χ^2 minimization. The best fit has a smaller χ^2 value (blue dashed line). Black circles represents and arbitrary sample of measurements⁷.

⁵Here α corresponds to the angle θ_{plane} in section 2.1.1.1

⁶<https://root.cern.ch/doc/master/classTMinuit.html>

⁷<https://www.phys.hawaii.edu/~varner/PHYS305-Spr12/DataFitting.html>

2.1.3.2 Kalman Filter

The Kalman Filter algorithm (KF) is a recursive least squares method to estimate the state of a dynamic system; its use is very common in navigation systems, as in the Global Positioning System (GPS). In high energy physics, Kalman Filter as a fitting method was first presented by Billoir in [31], but it can also be used in track finding and track vertexing process. The general theory of Kalman Filter is presented in the next paragraphs, followed by its specific application for MFT track-fitting.

Instead of a global fitting, such as the χ^2 -minimization, that uses all the measurements along several iterations, the Kalman Filter follow the system “point by point”, i.e., it fits the function measurement by measurement. This prevents operations with big matrices and allowing to treat material effects locally. To accomplish this process, Kalman Filter uses specific discrete points that represent the system at certain positions of interest. In the context of particle tracking, these points corresponds to hits at detection layers, which are used to update their respective coordinate vector representing the state vector of the system at that moment. Utilization of the KF in track fitting gives best estimations for parameters and covariance matrix, equivalent to other approaches using least-squares fit, but it is more efficient computationally-wise.

Kalman Filter is composed of two main steps, *prediction* and *update* (or *filtering*). Given an initial state, the estimation of the final state of interest is obtained by consecutive prediction and update steps. Parameters gets more precise at each cycle and after the final step, their estimations have information from all measurements. That way, one obtains the best estimation of the parameters and the corresponding covariance matrix at that last detector layer. Figure 13 illustrate this process; note that the Kalman Filter begins at the last particle cluster, processing hits in the opposite direction of the particle track. It’s also possible to use the full information to optimize the estimations at intermediate layers through the *smoothing* process. The next paragraphs describes in detail the *prediction* and *update* steps.

We can generically write the state vector \mathbf{p} describing a system of interest in layer k as a function of the state at a previous moment:

$$\mathbf{p}_k = \mathbf{f}_{k|k-1}(\mathbf{p}_{k-1}) + \boldsymbol{\delta}_{k|k-1}. \quad (2.28)$$

In the context of track fitting, \mathbf{p} represents the track parameters. Function \mathbf{f}_k represents the track propagator taking the track (state vector) from layer $k - 1$ to layer k ; its form will depend on the choice of the track model for the particle trajectory. $\boldsymbol{\delta}_{k|k-1}$ is a random variable representing the process noise and usually is a source of errors, e.g. Multiple Coulomb Scattering; $\boldsymbol{\delta}_{k|k-1}$ has covariance matrix \mathbf{Q}_k and does not necessarily affect the entire vector \mathbf{p} . The sub-index k goes from $k = 1, \dots, N$ where N is the number of detection layers.

Usually only a few elements of \mathbf{p} can be directly measured. Thus, in general we can write the measurements as a function of the track parameters as:

$$\mathbf{m}_k = \mathbf{h}_k(\mathbf{p}_k) + \boldsymbol{\epsilon}_k, \quad (2.29)$$

where function \mathbf{h}_k maps the track parameters to the measures and $\boldsymbol{\epsilon}_k$ represents the measurement errors with covariance matrix \mathbf{V}_k . Often \mathbf{h}_k is linear, so we can write \mathbf{m}_k as a linear

transformation:

$$\mathbf{m}_k = \mathbf{H}_k \mathbf{p}_k + \boldsymbol{\epsilon}_k; \quad \mathbf{h}_k(\mathbf{p}_k) = \mathbf{H}_k \mathbf{p}_k, \quad (2.30)$$

so that the mapping of parameters into measurements is performed by the measurement matrix \mathbf{H} . Following the same reasoning, if the propagator function \mathbf{f}_k is linear, a state \mathbf{p}_{k-1} can be taken to \mathbf{p}_k by a matrix \mathbf{F} :

$$\mathbf{p}_k = \mathbf{F}_{k|k-1}^{lin} \mathbf{p}_{k-1} + \boldsymbol{\delta}_{k|k-1}; \quad \mathbf{f}_{k|k-1}(\mathbf{p}_{k-1}) = \mathbf{F}_{k|k-1}^{lin} \mathbf{p}_{k-1}. \quad (2.31)$$

In the prediction step the state vector and its covariance matrix are propagated to next layer. In the case of a linear propagation, we can use (2.31) to propagate the parameters from layer $k-1$ to layer k , and the covariance matrix of the parameters $\mathbf{C}_{k|k-1}$ can be predicted using an exact linear error propagation:

$$\mathbf{p}_{k|k-1} = \mathbf{F}_{k|k-1}^{lin} \mathbf{p}_{k-1} + \langle \boldsymbol{\delta} \rangle, \quad (2.32)$$

$$\mathbf{C}_{k|k-1} = \mathbf{F}_{k|k-1}^{lin} \mathbf{C}_{k-1} \mathbf{F}_{k|k-1}^{lin T} + \mathbf{Q}_k. \quad (2.33)$$

However, in most cases \mathbf{f}_k is non-linear and it can be written as a function. Then, in general, the prediction from $k-1$ to k reads:

$$\mathbf{p}_{k|k-1} = \mathbf{f}_{k|k-1}(\mathbf{p}_{k-1}) + \langle \boldsymbol{\delta} \rangle, \quad (2.34)$$

$$\mathbf{C}_{k|k-1} = \mathbf{F}_{k|k-1} \mathbf{C}_{k-1} \mathbf{F}_{k|k-1}^T + \mathbf{Q}_k, \quad \mathbf{F}_{k|k-1} = \frac{\partial \mathbf{f}_{k|k-1}}{\partial \mathbf{p}_{k-1}} \Big|_{\mathbf{p}_{k-1}} \quad (2.35)$$

$\mathbf{C}_{k|k-1}$ is the predicted covariance matrix of $\mathbf{p}_{k|k-1}$, from $k-1$ to k , and it is the sum of the linear propagation of the covariance matrix of the last state \mathbf{C}_{k-1} plus the error matrix \mathbf{Q}_k that takes the material effects into account. For the specific case of MFT reconstruction, \mathbf{Q}_k is responsible for multiple scattering contribution and it is given by:

$$\mathbf{Q}_k = \begin{bmatrix} 0 & 0 & 0 & 0 \\ 0 & 0 & 0 & 0 \\ 0 & 0 & \sigma_{\theta_{plane}}^2 (\tan^2 \lambda_0 + 1) & -\sigma_{\theta_{plane}}^2 \left(\frac{q \tan \lambda_0}{p_{t_0}} \right) \\ 0 & 0 & \sigma_{\theta_{plane}}^2 (\tan^2 \lambda_0 + 1)^2 & -\sigma_{\theta_{plane}}^2 \left(\frac{q \tan \lambda_0}{p_{t_0}} \right) (\tan^2 \lambda_0 + 1) \\ 0 & 0 & -\sigma_{\theta_{plane}}^2 \left(\frac{q \tan \lambda_0}{p_{t_0}} \right) & \sigma_{\theta_{plane}}^2 \left(\frac{q}{p_{t_0}} \right)^2 \tan^2 \lambda_0 \end{bmatrix}, \quad (2.36)$$

where $\sigma_{\theta_{plane}}$ is given by equation (2.16):

$$\sigma_{\theta_{plane}} = \frac{0.0136 \text{GeV}/c}{\beta p} \sqrt{\frac{d}{X_0}} \left(1 + 0.038 \ln \frac{d}{X_0} \right),$$

and $\tan \lambda_0$ and q/p_{t_0} are MFT track-parameters. The exact forms of the track propagator $\mathbf{f}_{k|k-1}$ and its Jacobian matrix $\mathbf{F}_{k|k-1}$ depend on the choice of the track model and are given in subsection 2.1.1).

Now, with the predicted step $\mathbf{p}_{k|k-1}$ and measurements \mathbf{m}_k one can calculate the updated (or filtered) state $\mathbf{p}_{k|k}$:

$$\mathbf{p}_{k|k} = \mathbf{p}_{k|k-1} + \mathbf{K}_k \mathbf{r}_{k|k-1} \quad (2.37)$$

$$\mathbf{K}_k = \mathbf{C}_{k|k-1} \mathbf{H}_k^T (\mathbf{V}_k + \mathbf{H}_k \mathbf{C}_{k|k-1} \mathbf{H}_k^T)^{-1} \quad (2.38)$$

$$\mathbf{r}_{k|k-1} = \mathbf{m}_k - \mathbf{H}_k \mathbf{p}_{k|k-1}. \quad (2.39)$$

$\mathbf{r}_{k|k-1}$ is the residual difference between the predicted state for layer k and the measurement \mathbf{m}_k . \mathbf{K}_k is the Kalman gain matrix and have the role of weighting the contribution due the residual $\mathbf{r}_{k|k-1}$ in the estimation of $\mathbf{p}_{k|k}$. The covariance matrix for the updated state is:

$$\mathbf{C}_{k|k} = (\mathbf{I} - \mathbf{K}_k \mathbf{H}_k) \mathbf{C}_{k|k-1}. \quad (2.40)$$

The χ^2 quantity, used in statistical assessment of the fitting, can be calculated by:

$$\chi_k^2 = \mathbf{r}_{k|k-1}^T \mathbf{R}_{k|k-1}^{-1} \mathbf{r}_{k|k-1}, \quad (2.41)$$

$$\mathbf{R}_{k|k-1} = \mathbf{C}(\mathbf{r}_{k|k-1}) = \mathbf{V}_k - \mathbf{H}_k \mathbf{C}_{k|k-1} \mathbf{H}_k^T, \quad (2.42)$$

$$\chi_{total}^2 = \sum_{k=1}^N \chi_k^2, \quad (2.43)$$

where \mathbf{R} is the residual covariance matrix and χ_{total}^2 is the total χ^2 of the fitting.

After the update step, a new prediction step can be executed towards the next detection layer. The *prediction-update* cycle goes on until the last layer. Then, the final estimate state $\mathbf{p}_{k|k}$ will have information from all previous measurements and will have the best precision for the given set of observations. This is illustrated in figure 13.

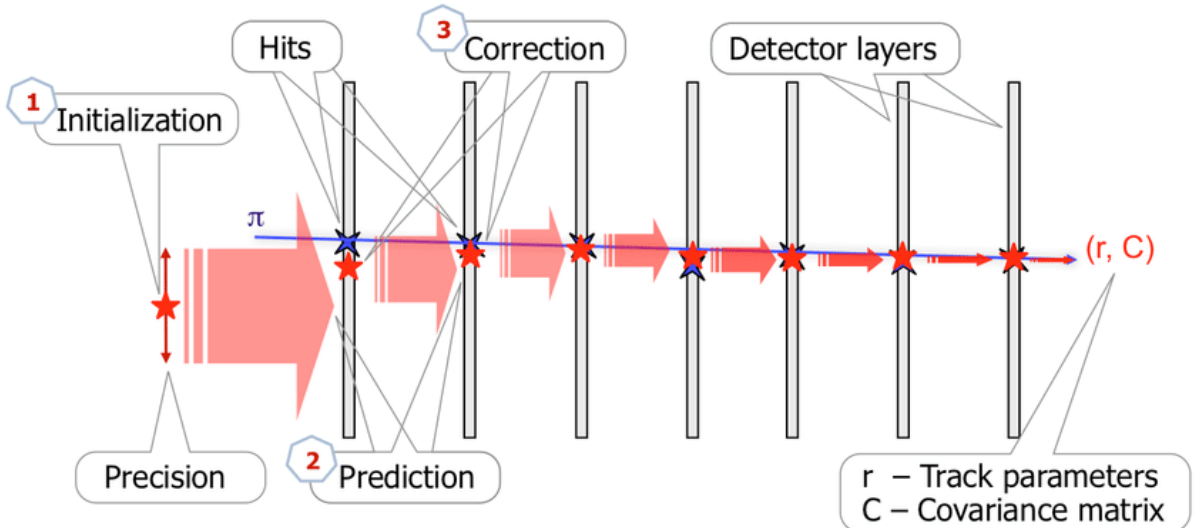


Figure 13: Illustration of the Kalman Filter algorithm, from [32]. It begins with an initial guess and poor precision, represented by the red arrow size. After each step, the filter outputs a corrected state between its prediction and the observable hits. As the filter predictions are corrected by measurements, its precision improves.

The Kalman Filter, in comparison to other least-square methods, has the advantage of not

having large-matrices operations, making the computational cost depend mainly on the number of detection layers. Also, linear approximations may have a better performance, since it only needs to be valid between two consecutive layers and not the entire track length.

More details on the Kalman Filter algorithm can be found in the paper by Frühwirth [33] and also in the *Data analysis techniques for high-energy physics* book by Frühwirth, Regler, Bock, Grote and Notz [25] (or [34]).

A challenge in implementing the KF is to find a good “seed”, i.e., the initial values of the filter for the state $k = 0$. Measurements in the first layer can be used to obtain some of the initial values. In the specific case of MFT Kalman Filter, the first measurement can be directly used as x and y parameters of \mathbf{p}_0 ; having another measurement, the ϕ and $\tan \lambda$ of \mathbf{p}_0 can be calculated. The seed of the final parameter of \mathbf{p}_0 , q/p_t , is given by a conformal transformation [29]. Since the initial guess for the KF are obtained from the measurements, in order to not use information from the observations twice, we must set big values in the covariance matrix C_0 . If the seed for covariance matrix is too big, the KF may fail to reach a desirable error. But if the seed for covariance matrix is too small, it can “lock” the filter, not letting it to update track-parameters accordingly to the new measurements. How “big” this values can be may depend on the system and to find the optimal seed may require some fine tuning.

2.2 Quality control of reconstructed track parameters

Through track reconstruction, one can retrieve essential information for an experiment physics program. Naturally, the tracking process must be reliable, describing the particle trajectory in an accurate way, to not compromise future physics analysis. In order to study the quality of MFT track reconstruction, we analyze the following quantities:

- vertex-coordinates resolutions;
- q/p_t resolution;
- standard deviations of track-parameters normalized residuals (*pulls*).

Vertex resolution defines the tracking capabilities of the MFT and is the most important quantity, since it is directly related to the main objectives of the detector. The pulls will give information about the accuracy of the track-parameters errors estimation, important for MFT-MCH track matching, and of the fitting quality itself.

The position resolution $\sigma(x,y)$ can be evaluated with respect to the residuals $r_{x,y}$ of the estimated vertex coordinates of the fitted track and the Monte Carlo vertex position.

$$\sigma(x,y) = \sigma(r_{x,y}), \quad (2.44)$$

$$r_x = X_{fit} - X_{MC} \quad (2.45)$$

$$r_y = Y_{fit} - Y_{MC}. \quad (2.46)$$

The resolution of the inverse transverse momentum $\sigma(q/p_t)$ is given in terms of the relative

error:

$$\sigma(q/p_t) = \sigma \left(\frac{r_{q/p_t}}{(q/p_t)_{MC}} \right) \quad (2.47)$$

$$r_{q/p_t} = (q/p_t)_{fit} - (q/p_t)_{MC} \quad (2.48)$$

The *reduced* or *normalized residuals*, also called *pulls*, are the residuals of the track parameters normalized with respect to the estimated error σ of that parameter [25, p. 326]:

$$r_{pulls} = \frac{\mathbf{p} - \mathbf{p}^t}{\sigma(\mathbf{p})} \quad (2.49)$$

\mathbf{p} and \mathbf{p}^t are the estimated parameters from the fitting and the true parameters (known from MC simulations), respectively. The *Pull* is one of the main quantities in evaluating a fitting process (the other one being the χ^2). The parameters pulls are related to the track model, covariance matrix estimation and functionality of the track-fitting in the reconstruction algorithm. If the fitting process is successful, the pulls distribution will have mean zero and standard deviation one. Figure 14 shows a pull distribution, for the x position track-parameter, and their fitted standard deviation.

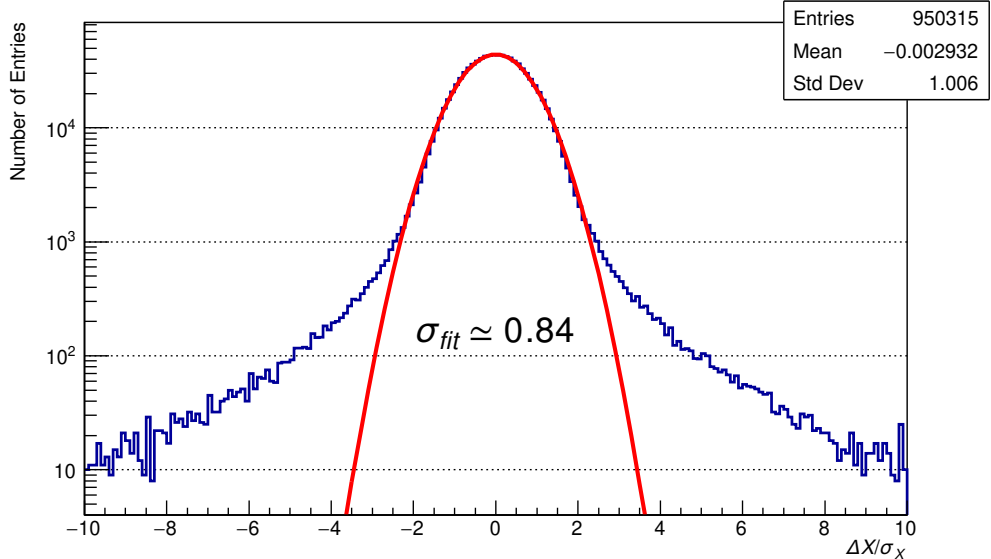


Figure 14: Histogram of the X parameter reduced-residuals (pulls) integrated in p_t and η . σ_{fit} is the pull standard deviation obtained from a Gaussian fit (red line) using ROOT’s built-in fitter.

To realize assessment of MFT track reconstruction, plots of the vertex coordinates resolutions, q/p_t resolutions and pulls standard deviations for MFT parameters ($x, y, \phi, \tan \lambda, q/p_t$), as functions of transverse *momentum* p_t for different ranges of the pseudo-rapidity η are used. All quantities are evaluated with respect to the vertex position, having the Monte Carlo parameters as reference. A differential plot with respect to p_t allows a detailed assessment concerning different effects impacting the reconstruction, e.g. multiple scattering. Plotting the standard variation of the pulls, it is possible to estimate the compatibility of the fitted covariances and the actual errors. If estimated covariances are too high, then the pull standard

deviation will be low ($\sigma(r_{pulls}) < 1$); on the other hand, a high standard deviation of the pull ($\sigma(r_{pulls}) > 1$) means that the estimated error are too low.

Using the quantities mentioned above, we addressed the following topics:

- fitting methods: χ^2 -minimization and the Kalman Filter fitting methods were evaluated, comparing reconstructed tracks;
- track-models: the exact helix track model was compared with a second order expansion approximation (quadratic model) and first order approximation (linear model);
- cluster resolution: single pixel resolution and cluster resolutions from statistical analysis were compared.
- material budget: track reconstruction was made using different values for MFT’s material budget, in order to optimized track fitting.

The practical implementation of this track-reconstruction quality assessment is discussed in section 3.2.

2.2.1 Computational tools

ALICE O²: The O² software framework⁸ is ALICE’s online-offline computational environment responsible for data workflow in the experiment. It was developed to deal with the increased data flux due to the experiment upgrade for RUN 3, comprising upgrades of online systems, related to triggering and data acquisition, and of offline stages of track reconstruction and data analysis. Starting at RUN 3, ALICE will begin to work with a continuous flux of data (instead of select events by triggering), with rates up to 50Hz for Pb-Pb collisions, resulting in a flux of approximately 3 Tb/s. The ALICE O² software repository also contains all the necessary code for reconstruction, calibration and simulation for the ALICE experiment in RUN 3.

All simulations and track-reconstruction processes are executed through ALICE O². Simulations samples can be generated using Monte Carlo generators, as the Pythia event generator⁹, or through more flexible generic generators, where the simulation parameters can be adjusted at will. Also within ALICE O² are the Geant 4 simulation toolkit, in charge of simulating the transport of particles through the experiment. The ROOT framework for data analysis is also integrated in ALICE O² and it was the main working tool used in this work. ROOT is presented in the next paragraph.

ROOT Framework ROOT is a data analysis framework for high energy physics created at CERN¹⁰. ROOT was written in C++ and although it is the main programming language, ROOT have interfaces with other languages, such as Python and Ruby. ROOT counts with several packages to aid in data analysis; among those package we can cite: packages for histogram creation, matrix algebra operations, multivariate data analysis (including machine learning), curve fitting (regression analysis) and other statistics tools used for data analysis.

⁸<https://github.com/AliceO2Group/AliceO2>

⁹<https://pythia.org>

¹⁰<https://root.cern>

The tools implementing the quality assessment presented in section 2.2 were created using the O²-ROOT integration. Programs were written in C++ and several ROOT libraries. The plots presented in this work were also made within the ROOT framework.

The computational infrastructure required to execute simulations, reconstruction and data analysis was provided by PCAD-INF/UFRGS and GEFAE-IF/UFRGS.

CHAPTER 3

DEVELOPMENT, RESULTS AND DISCUSSION

This chapter presents the development and implementation of the present work, as well as the main results and discussions. Initially the tools developed to execute the quality control of the reconstructed tracks will be described, followed by the standard configurations used in assessment and simulations. In a second moment, we show our results: i) comparison between track reconstruction using different track models - helix, quadratic and linear models; ii) comparison between fitting methods with the Kalman Filter and χ^2 -minimization; effects on reconstruction of iii) cluster uncertainties and of iv) material budget. Three samples of Monte Carlo (MC) simulations are used in this work:

1. muons with uniform *momentum* and pseudo-rapidity distribution are used to compare different reconstruction methods with uniform statistics within the phase-space;
2. muons and pions (also with uniform distributions of p and η), in order to demonstrate that the reconstruction is not sensitive to particle species;
3. a Pythia proton-proton (pp) MC sample illustrates that the results obtained with the muon samples are representative of realistic physics cases.

The Pythia generator is a Monte Carlo event generator which is capable of simulate high-energy physics collision events. As such, it produces a wider range of particle types compared to the other samples. Pythia standard configuration produces particles in a narrow range of p_t ; for this reason, the sample with only muons was chosen as the main sample, since the flexibility of its “box” generator allows the analysis in a wider p_t range.

The basic settings for the simulation of muon samples (cases 1 and 2) are:

- pseudo-rapidity range: $-3.8 < \eta < -2.3$;
- *momentum* range: $(0.01 < p < 400)$ GeV/c;
- standard deviation of the z coordinate vertex distribution = 5.

For the pure muon case, the sample was produced with 5000 events with 500 muons per event. For the muon and pion case, the simulation produced 5000 events with 200 muons and 200 pions. The Pythia simulation followed a standard built-in configuration with 50000 events.

In the reconstruction workflow, a search radius of 0.0100 cm around the seed line is set for the Linear Track Finder track-finding algorithm (see appendix A). The simulation sample

was created with a generic “box” generator, with a flat p_t distribution. This flat distribution allows the assessment of muon track with higher transverse *momentum* in comparison with the Pythia generator. After the presentation of the main results, the track-reconstruction on the pure muon sample is compared with reconstruction on more complex samples, in order to extend the validity of this study.

3.1 Simulation and reconstruction

Simulation process in ALICE software is divided in 3 main steps: i) generation of particles and simulation of chosen detectors (their geometry and other physical features); ii) conversion of the simulated hits to detector digits and; iii) reconstruction. In each step, the user can selected any number of ALICE’s detectors, according to the analysis objective. For this work, the only detector simulated was the MFT, since the analysis is focused on the MFT standalone track-reconstruction.

The first step simulates particles and detectors as defined by the user. From the collision simulation, the particles are transported through the selected detectors by the Geant4 toolkit. The second step, known as “digitization”, converts the simulated hits to digits, identifying fired pixels. After this, information from simulated or real data is not distinguishable anymore, and the same workflow is used both for simulations or real collisions. The final step is responsible for taking detectors digits and group them into clusters, which will be used through the rest of the reconstruction process. After that reconstruction continues with the track-finding and track-fitting process. The assessment of reconstruction is integrated in this step as well.

3.2 Assessment of track-reconstruction

The quality control of reconstructed tracks at the MFT is performed using the MFT reconstruction assessment workflow.

In order to qualify MFT track reconstruction, one needs to evaluate position and *momentum* resolutions. This can be achieved by observing the following quantities:

- Vertex X-coordinate offset resolution;
- Vertex X-coordinate offset pull distribution;
- q/p_t resolution;
- q/p_t pull distribution.

As mentioned in section 2.2, these quantities are plotted as functions of the transverse *momentum* (section 3.3). The quantities are evaluated at the estimated vertex position. The corresponding state-vector is estimated from the analytical propagation of the fitted track to the Monte Carlo vertex z-position, i. e., from the first detector layer to the interaction point. Then, using the state vector at this position, the resolutions and pulls are evaluated, having the Monte Carlo parameters as reference.

By observing the plots of the quantities mentioned before, we addressed the track-reconstruction topics presented in section 2.2. This is realized by comparing different configurations for each topic. These configurations are summarized in table 2.

Fitting model		Experimental parameters	
Track model	<ul style="list-style-type: none"> • Helix model • Quadratic model • Linear model 	Cluster Resolution	<ul style="list-style-type: none"> • Cluster dictionary • single pixel
Fitting method	<ul style="list-style-type: none"> • Kalman Filter • χ^2 -minimization 	Material Budget (per disk)	<ul style="list-style-type: none"> • 0.042 radiation length • 0.084 radiation length • 0.126 radiation length

(a)

(b)

Table 2: Track reconstruction topics addressed in this work (left columns) and their respective configuration options used for comparisons (right columns). Table (a) shows fitting models; table (b) shows the adjustable experimental parameters.

Track-reconstruction default configurations

Different configurations for track-reconstruction were tested, changing one element of table 2 at a time, in order to clearly visualize the impact of different configuration parameters. With that in mind, it is useful to define a default configuration for the MFT track-reconstruction for this study¹. Results shown will generally have the following reconstruction settings: Kalman Filter as fitting method, following the MFT technical design report [27]; helix model as track model, since it is the theoretical model describing a particle motion within MFT region; the cluster dictionary used is the one uploaded at the Condition and Calibration Data Base (CCDB), which was created using data from LHC pilot beam (in October, 2021); lastly, the choice of the nominal MFT radiation length ($0.042\% x/X_0$) is also a natural choice for the standard value of the material budget.

Noteworthy, the studies of the reconstruction configurations were performed with no specific order. The reconstruction assessment aided in finding errors and bugs in the reconstruction algorithms. Correction of these bugs and other improvements contributed (and still do) to the ongoing improvement of the O² framework. Here, the studied topics were arranged trying to follow a logical order, where the essential points of reconstruction are presented first.

¹This does not mean this “default configuration” is universal, as O² itself may have other setting. It is defined as such to have a common ground and facilitate the comparison presented here.

3.3 Results

Results from this work are organized as follows. First, results regarding the fitting model with comparisons of track reconstruction using different track models and different fitting methods are presented. Then the influence of the cluster topology and the material budget on the fitting are shown.

Below, considerations on the plots presented in this chapter are discussed, in order to clarify their interpretation:

- vertex resolution: the vertex resolution is based on the x and y residuals (equation (2.44)). Resolution is asymptotically better as higher the p_t , since these tracks are less affected by material effects.
- q/p_t resolution: here the resolution is given with respect to the relative error, so we can read the y-axis percent-wise.
- parameters $\sigma(pulls)$: the standard deviation of a parameter pull is related to the estimation of that parameter covariance matrix. As discussed in section 2.2, the standard deviation of a pull should be equal to one. Values above one means the pull distribution is too wide, either because the residuals are smaller or because the estimation of the error has a low value (or both). Values below one means that the error values are too high, resulting in narrow distributions.

3.3.1 Comparisons of track models and fitting methods

3.3.1.1 Comparison between helix track model and approximations

Although the helix track model is the ideal theoretical model describing a particle trajectory in the MFT region, its mathematical treatment is not straightforward, specially regarding its Jacobian (2.11). Here we present comparisons of the helix model with the track approximations of second and first order expansions, with the intention of describing the MFT tracks in a simpler way, but still valid for the experimental conditions.

Helix track model vs quadratic approximation

Figure 15 shows the comparisons of the helix and quadratic track models for MFT reconstruction. Configuration for the other reconstruction parameters are:

- fitting method: Kalman Filter;
- cluster resolution: cluster dictionary;
- material budget: $0.042 x/X_0$ (nominal MFT value).

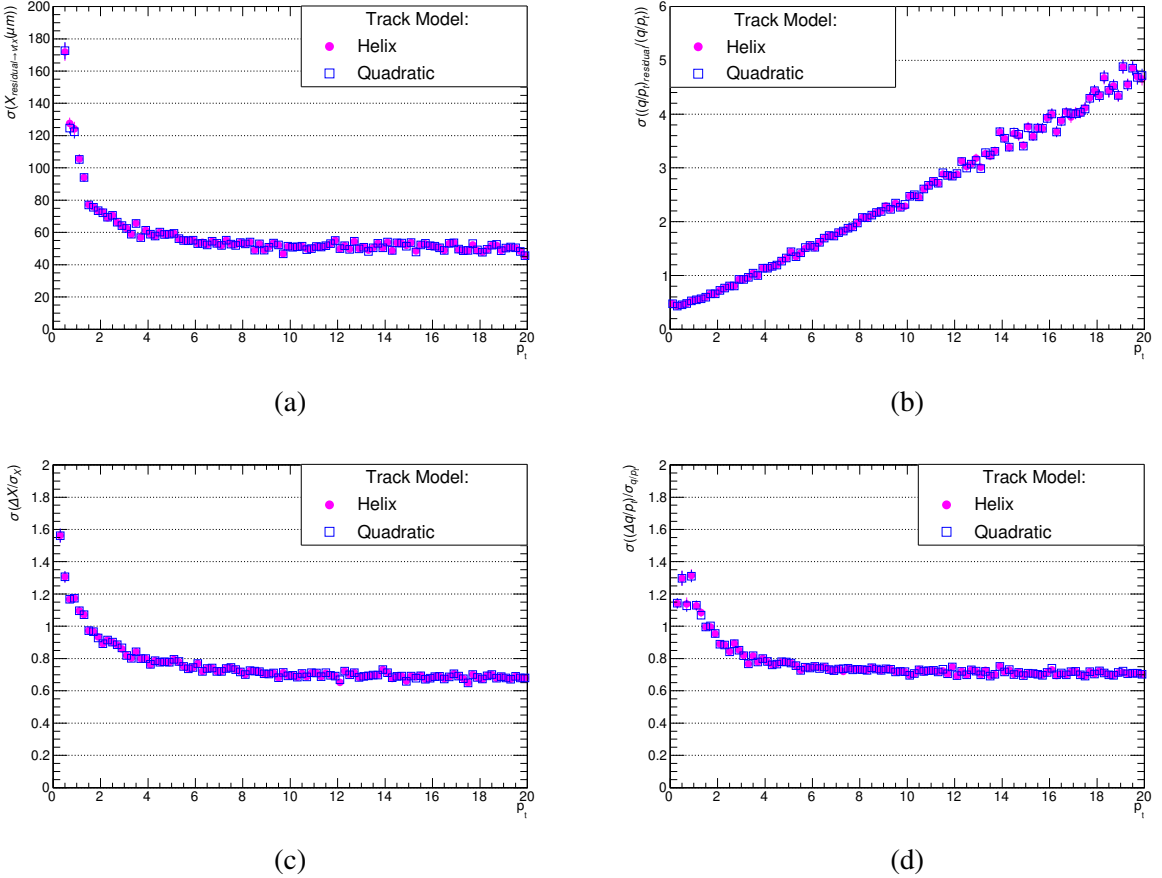


Figure 15: Comparison between helix track model and quadratic track model (second-order approximation) for pseudo-rapidity range of $-3.0 < \eta < -2.8$. Reconstruction configurations: fitting method: Kalman Filter; cluster resolution: cluster dictionary; material budget = 0.042 x/X_0 . (a) resolution of the vertex x coordinate; (b) q/p_t resolution; (c) pulls standard deviation for vertex x coordinate; (d) pulls standard deviation for q/p_t .

First, as a general result, the worse resolution of q/p_t at high p_t is due to the fact that the first q/p_t estimation is based on the track curvature and the tracks are more linear as higher the p_t . This will be seen in all the forthcoming plots.

About the specific comparison, no significant differences in the results can be seen, meaning that in MFT running conditions, reconstruction with the quadratic approximation could be used instead of the helix model.

The possibility of being able to use the quadratic Jacobian, allows a better understanding of the error correlations, in addition to having a lower computational cost.

Helix track model vs linear approximation

Figure 16 shows the comparisons of the helix and linear track models for MFT reconstruction. Note that a linear model does not account for the inverse charged transverse *momentum* parameter, since it is the source of track curvature, which is not addressed in such a track model. Because of this, the charged *momentum* comparisons will be omitted in the present section.

The other reconstruction configurations are the same as before:

- fitting method: Kalman Filter;
- cluster resolution: cluster dictionary;
- material budget: $0.042 x/X_0$ (nominal MFT value).

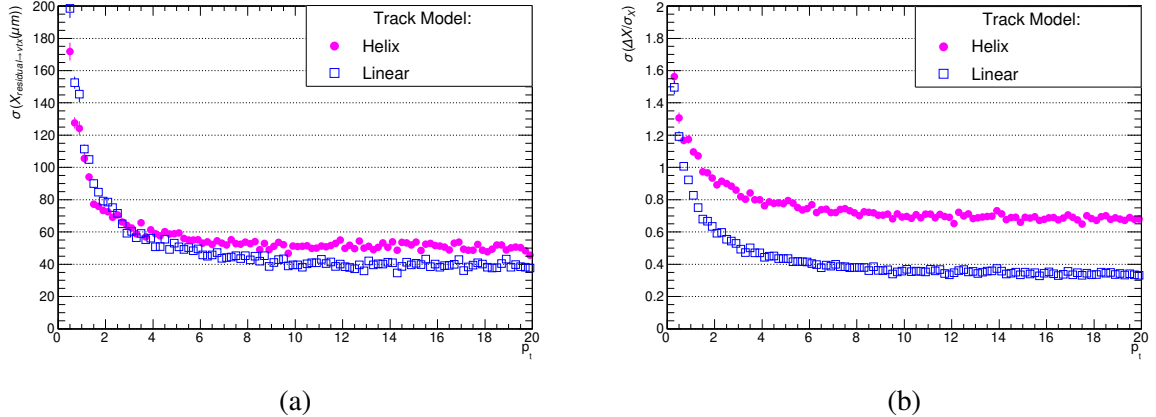


Figure 16: Comparison between helix track model and linear track model (first-order approximation), for pseudo-rapidity range of $-3.0 < \eta < -2.8$. Reconstruction configurations: fitting method: Kalman Filter; cluster resolution: cluster dictionary; material budget = $0.042 x/X_0$. (a) resolution of the vertex x coordinate; (b) pulls standard deviation for vertex x coordinate.

Figure 16a shows the linear model outperforms the helix model for $p_t \gtrsim 2.5$ GeV, increasing the difference as higher the p_t to a value up to $\approx 10 \mu\text{m}$. This may happen because of fitting instabilities provoked by the fitting of q/p_t , which need information from the muon spectrometer (absent here) to be better estimated, specially at higher p_t , where the estimated transverse *momentum* is worse, since tracks tends to be straighter. In the low p_t range, the helix model presents better results, as it is expected, since in this region the field effects are more prominent, causing a more curved track.

With the linear track model the standard deviations of the pulls is far from ideal, as can be seen in figure 16b, meaning the fitting is not estimating the errors accordingly.

The comparison just presented allows to define a “high p_t ” region for the MFT reconstruction, that is, when the vertex resolution is better ($p_t \gtrsim 2.5$ GeV). Therefore, the linear model would be preferable in this regime, even though the error estimation is not better, since it is the vertex resolution that addresses the main physics topics of MFT. One should remember, however, that the results shown here concerns MFT standalone tracks, and shall be extrapolated with caution if considered in other detectors reconstructions.

3.3.1.2 Fitting methods: Kalman Filter and χ^2 -minimization

Now we present a comparison between two fitting methods applied to MFT track reconstruction. Figure 17, shows a comparison between the Kalman Filter for track fitting

and the χ^2 -minimization method. The quadratic track model was used in both methods, since it allows a much simpler implementation (specially regarding χ^2 -minimization), without compromising the representation of the particle trajectory. The comparison test had the goal of aiding KF optimization. The other reconstructions configurations follows:

- track model: quadratic;
- cluster resolution: cluster dictionary;
- material budget: $0.042 x/X_0$ (nominal MFT value).

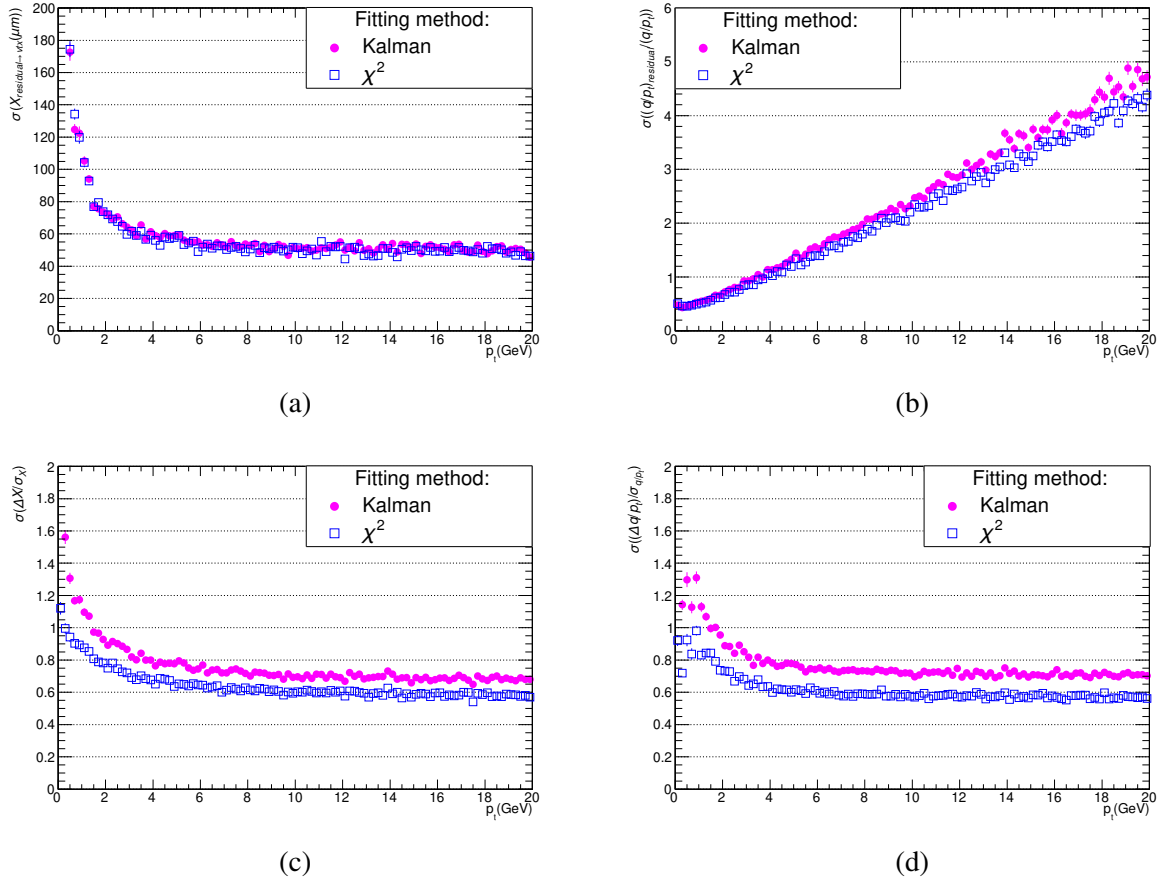


Figure 17: Comparison between track-fitting methods Kalman Filter and χ^2 -minimization, in MFT track reconstruction, for pseudo-rapidity range of $-3.0 < \eta < -2.8$. Reconstruction configurations: track model: quadratic; cluster resolution: cluster dictionary; material budget = $0.042 x/X_0$. (a) resolution of the vertex x coordinate; (b) q/p_t resolution; (c) pulls standard deviation for vertex x coordinate; (d) pulls standard deviation for q/p_t .

Using the same initial configuration, it can be seen that both methods achieve very similar vertex resolutions (figure 17a) and a slight advantage for the χ^2 -minimization in the transverse momentum resolution (figure 17b). This suggests that further fine tuning of Kalman Filter's seed parameters can be performed.

We can see in plots 17c and 17d, that the errors estimation depends on p_t . For low p_t the χ^2 -minimization is closer to the unity, but it is asymptotically worse than Kalman

Fitter. However, the most limiting factor of the χ^2 method is the computational time. It took approximately twice as long for the χ^2 -minimization to converge in comparison with the KF fitting. MFT track reconstruction shall be done on the fly, and the MFT detector will be dealing with a huge amount of tracks, so the fitting shall be as fast as possible.

3.3.2 Experiment parameters

3.3.2.1 Cluster topology resolution effects

This section presents the effects of considering different cluster errors for different cluster topologies in the MFT track reconstruction. Comparisons were done using the standard deviation of hits obtained from the nominal single pixel resolution and obtained from a cluster dictionary, which associates each different cluster topology with a corresponding cluster resolution (see section 2.1.2). Resolution from a single pixel is given by: pitch/ $\sqrt{12}$, where the sensor's pitch $\approx 25 \mu\text{m}$. In the cluster dictionary, multi-pixel clusters can achieve resolutions below $3 \mu\text{m}$ and mean values of $6.4 \mu\text{m}$ for x coordinate and of $7.1 \mu\text{m}$ for the y coordinates. The other configurations used in these reconstructions are:

- track model: helix;
- fitting method: Kalman Filter;
- material budget: $0.042 x/X_0$ (nominal MFT value).

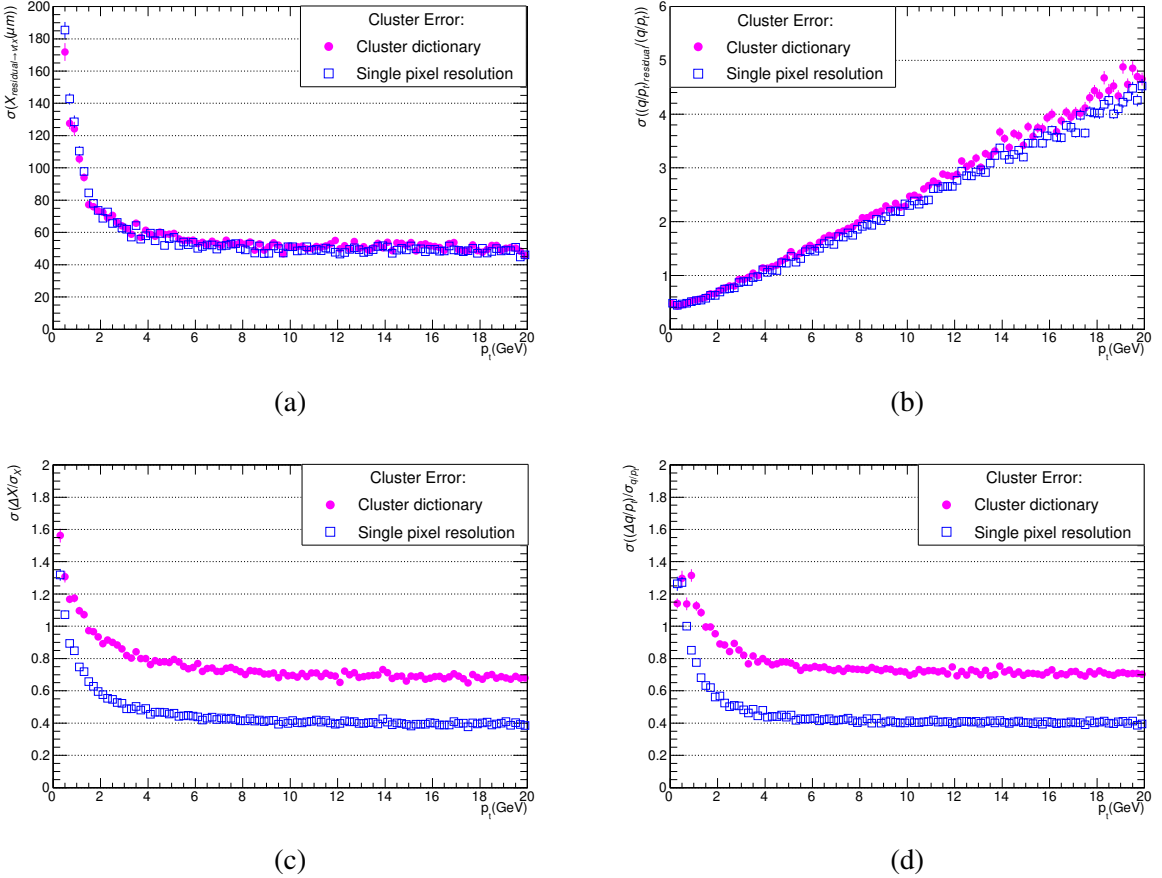


Figure 18: Effect of the use of cluster dictionary on MFT track fitting, for pseudo-rapidity range of $-3.0 < \eta < -2.8$. Reconstruction configurations: track model: helix; fitting method: Kalman; material budget = $0.042 x/X_0$. (a) resolution of the vertex x coordinate; (b) q/p_t resolution; (c) pulls standard deviation for vertex x coordinate; (d) pulls standard deviation for q/p_t .

Figure 18 shows very similar resolutions. There is a slight advantage in offset resolution (figure 18a) if using a cluster dictionary (low-\$p_t\$ region), but also a slightly worse q/p_t resolution (figure 18b); still, most differences are within error bars. Figures 18c and 18d show the impact of using a cluster dictionary containing different errors for each cluster topology on the fitting process. The use of a dictionary improves the error accuracy, as one would suspect, demonstrating that the effective resolution is indeed better than the resolution of a single pixel.

3.3.2.2 Material budget effects

This section presents the effects of the radiation length of the MFT in track reconstruction - figure 19. We limit the comparison using values of material budget that do not greatly deprecate resolutions. Furthermore, figures 19a, 19c and 19d had the p_t axis shorten, in order to better visualize the comparisons (no difference was seen for $p_t > 5$ GeV). It is worth mentioning that the MFT geometry when of the simulation is unchanged, only the value at the reconstruction step is affected. Besides the material budget value, the other configurations used in these reconstructions are:

- track model: helix;
- fitting method: Kalman Filter;
- cluster resolution: cluster dictionary.

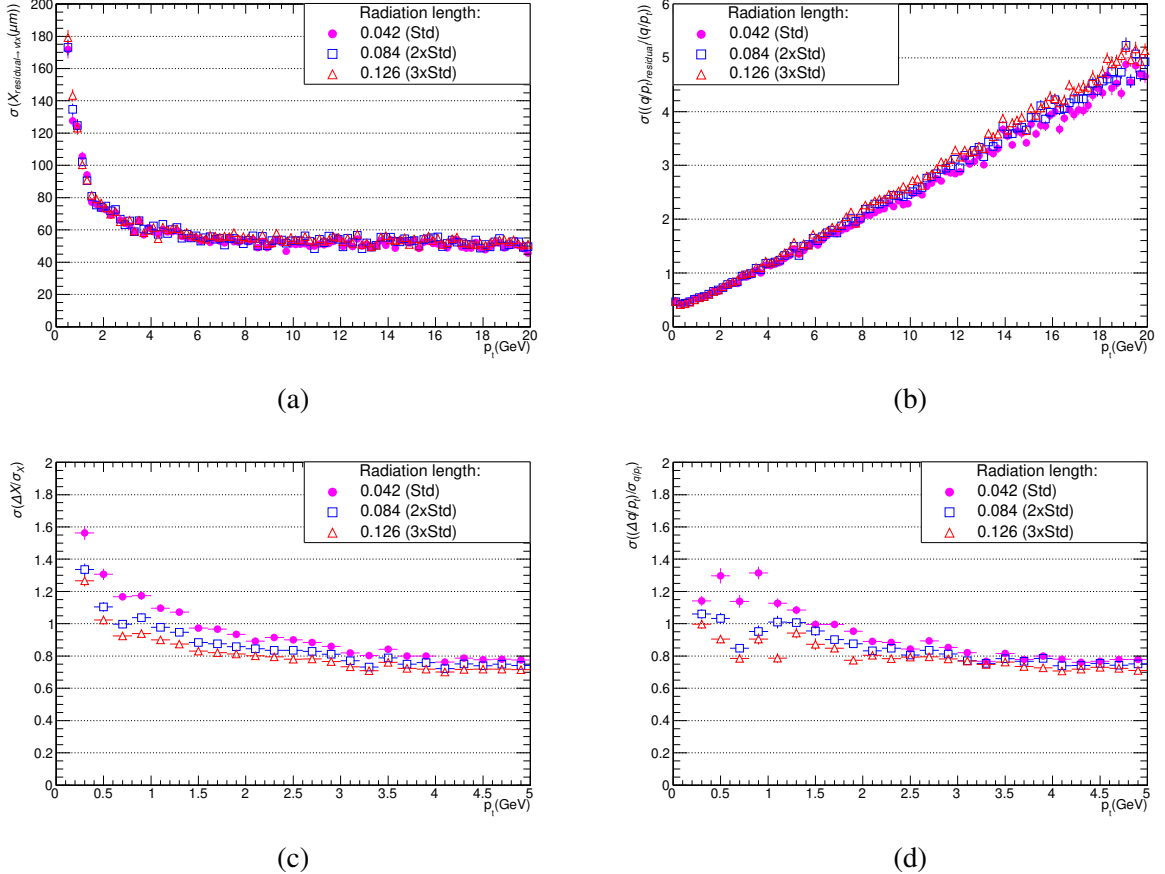


Figure 19: Effect of different radiation lengths in MFT track fitting, for pseudo-rapidity range of $-3.0 < \eta < -2.8$. Reconstruction configurations: track model: helix; fitting method: Kalman; cluster resolution: dictionary. (a) resolution of the vertex x coordinate; (b) q/p_t resolution; (c) pulls standard deviation for vertex x coordinate; (d) pulls standard deviation for q/p_t .

There is no significant difference in offset resolution for the plotted values of the radiation length (figure 19a); regarding the transverse *momentum* resolution (figure 19b), it seems increasing the material budget worsens the resolution, but most values are within error bars.

Looking at figures 19c and 19d we see that, as one would expect, the effects are more prominent at low the p_t , since this region suffers more from the multiple scattering effects. The results show that using two times the nominal MFT material budget should be considered when doing the reconstruction process, since it provides better error estimations (standard deviation of pulls close to the unity). This results may be explained by the use of MFT's mean material budget as nominal value in the track-reconstruction, suggesting the calculation of the material budget using the root mean square should be more appropriated.

3.3.2.3 Other event topologies

The results presented so far are based on a simple simulation containing only muons, which is the particle of interest to be identified by ALICE's muon spectrometer. In order to validate this study regarding actual collisions, this section presents a comparison between the sample used in the previous results with two other, more complex, samples:

- i) 5000 events with 200 muons and 200 pions;
- ii) 50000 events using the Pythia generator with pp collisions.

Reconstruction configurations are:

- track model: helix;
- fitting method: Kalman Filter;
- cluster resolution: cluster dictionary;
- material budget: $0.042 x/X_0$ (nominal MFT value).

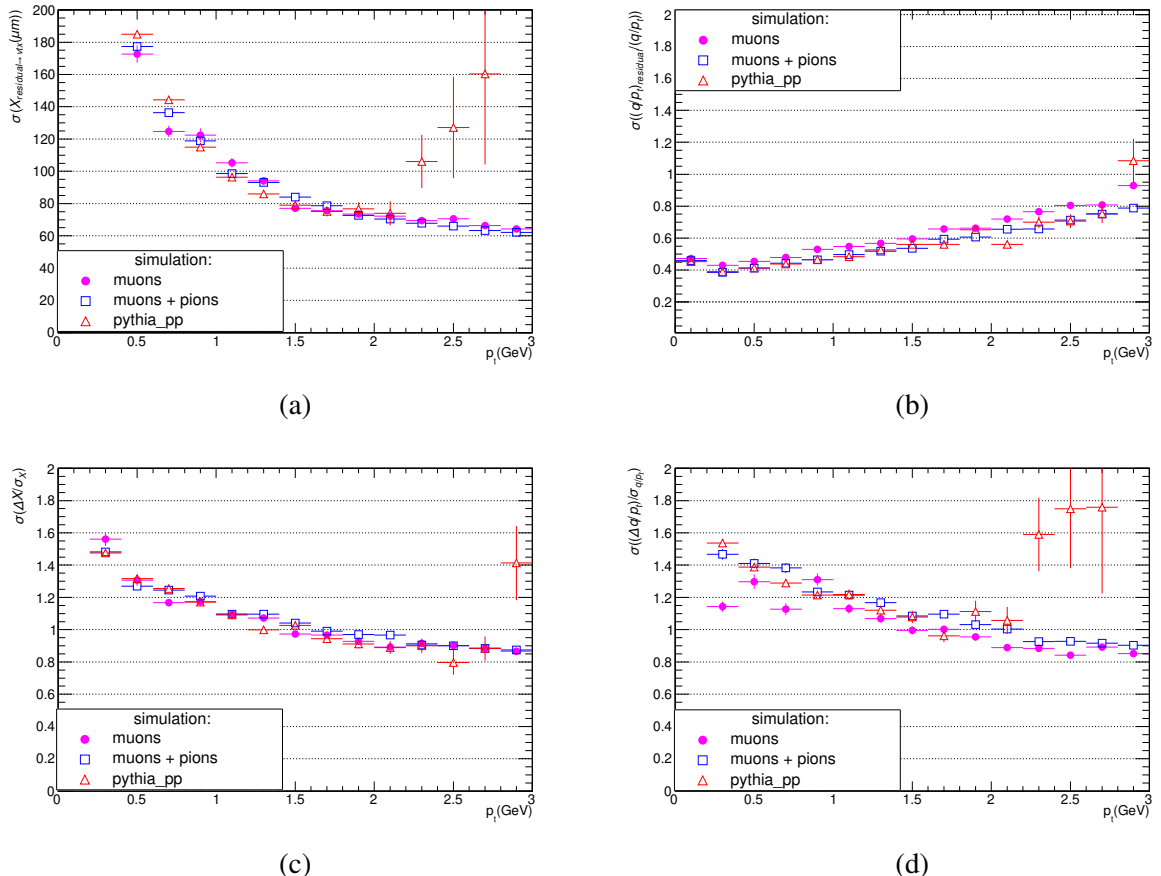


Figure 20: Comparison of “box” simulation samples with a Pythia pp sample, for transverse momentum range of $0 < p_t < 3$ and pseudo-rapidity range of $-3.0 < \eta < -2.8$. Reconstruction configurations: track model: helix; fitting method: Kalman; cluster resolution: dictionary. (a) resolution of the vertex x coordinate; (b) q/p_t resolution; (c) pulls standard deviation for vertex x coordinate; (d) pulls standard deviation for q/p_t .

We see from the four plots on figure 20 that the results are comparable for all samples. For p_t above 2 GeV, the lack of statistics of the Pythia sample becomes visible, as indicated by the large error bars in figures 20a and 20d. Still, the other two samples (muon and muon plus pion) keeps their good agreement.

The results shown here indicates that the analysis performed on the muon sample can be used to assess MFT's reconstructed tracks in more realistic scenarios, as simulated by the Pythia generator.

Results summary

Following the discussions above, we can summarize the presented results as follows:

- Figure 15 shows that the quadratic model approximation is practically identical in describing MFT tracks as compared to the full helix track model. Using the quadratic model reduces computational cost of track propagation without compromising the quality of reconstruction, so it can be used as the default track model in MFT track reconstruction, without compromising the quality of physics analysis;
- from figure 16a, it is seen the linear model approximation may be considered in vertexing at high p_t , since particles move closer to a straight line, as it has shown lower offset resolution in this region;
- in figure 17, χ^2 -minimization presents a slightly better transverse *momentum* resolution and comparable pulls at low p_t in relation to the Kalman Filter, which indicates the existence of room for improvement regarding KF. In tests made during this work, no other configuration could improve q/p_t resolution keeping the quality of vertex resolutions and pulls;
- figure 18 shows that MFT track reconstruction using cluster resolutions based on the effective resolution for each cluster topology provides better errors estimation compared to the reconstruction using resolutions of a single pixel;
- results on figure 19 reveal that MFT track reconstruction achieves improved estimation of track-parameters uncertainties by considering $x/X_0 = 0.084$ for the MFT. This is twice the average radiation length of the MFT and could be considered as the default configuration for MFT track reconstruction. The use of the average MFT radiation length for all MFT disks, instead of a RMS calculation, may explain this difference;
- Figure 20 indicates that studies using pure muon simulations are also valid for other particle species and event topologies.

CHAPTER 4

CONCLUSION

This work studied charged particle-track reconstruction at forward geometries and its application to current experimental setups of the Large Hadron Collider, in specific, the Muon Forward Tracker of the ALICE experiment. State of the art tracker detectors were presented after a brief introduction to key particle detection technologies. Then followed a description of physical concepts and challenges associated to the estimation of particle-track parameters and its uncertainties, where Kalman Filter is the standard method in the field. The present work also shows open topics regarding the strategy of MFT track reconstruction, as the algorithm used in track fitting and the fine tuning of cluster resolutions for better high p_t resolutions. These point should be clarified in future works, in order to have the best possible use of the data obtained by the detector.

Results based on Monte Carlo simulations indicate that at forward geometries the quadratic approximation is a suitable approximation for a forward detector with ten detector planes immersed in an uniform magnetic field of 0.5 T parallel to the detector axis. At this weak field geometry the tracker has a very poor charged momentum resolution. However, under these conditions its tracking capabilities are very good, having position resolution around 100 μm at $p_t \approx 1 \text{ GeV}$ and of 50 μm for $p_t > 5 \text{ GeV}$.

The better results achieved by the χ^2 fitting method, specially regarding q/p_t resolution at high p_t , could decisively affect the track matching between the track of MFT and the muon spectrometer. Thus, in despite of the higher computational cost, the χ^2 -minimization method could be considered for MFT track reconstruction.

Also, the improvement of resolution leads to lower residuals between the fitted track parameters and the Monte Carlos values generated for the simulation, implying lower pulls, as observed.

Deviation from the unity of the pulls standard deviation at low p_t can be reduced by fine tuning the radiation length x/X_0 of the MFT to twice the average material budget of the MFT. At high transverse *momentum* there is room for improvement, which may be achieved by fine tuning the cluster resolution. As the fine tuning of x/X_0 resulted in better pulls at low p_t , in a similar way, a fine tuning in cluster resolutions must be considered for improving results at high p_t regions.

Finally, the study performed here had the goal of qualifying MFT track reconstruction. The development of this work produced contributions to the MFT standalone reconstruction and subsidies MFT reconstruction strategy chosen for the RUN 3 of data taking. Still, the decision regarding the reconstruction strategy adopted by MFT, must also be based considering the matching performance with the muon spectrometer tracks and the track-parameter quality of the resulting tracks. Track-matching between the MFT and the muon spectrometer is beyond

the scope of this investigation. Nevertheless, the strategy and tool outlined in this work are equally valid for the assessment of global muon tracks, and are actually in production.

The track assessment tools developed for this study are included in ALICE online-offline computing system, the ALICE O², as part of the MFT assessment workflow and is already used in the RUN 3 of the LHC.

Bibliography

- [1] J. J. Thomson. Cathode rays. *Phil. Mag. Ser. 5*, 44:293–316, 1897.
- [2] Carl D. Anderson. The positive electron. *Phys. Rev.*, 43:491–494, Mar 1933.
- [3] S. H. Neddermeyer and C. D. Anderson. Note on the Nature of Cosmic Ray Particles. *Phys. Rev.*, 51:884–886, 1937.
- [4] C. M. G. Lattes, G. P. S. Occhialini, and C. F. Powell. Observations on the Tracks of Slow Mesons in Photographic Emulsions. 1. *Nature*, 160:453–456, 1947.
- [5] G. Arnison et al. Experimental observation of isolated large transverse energy electrons with associated missing energy at $s=540$ gev. *Physics Letters B*, 122(1):103–116, 1983.
- [6] M. Banner et al. Observation of single isolated electrons of high transverse momentum in events with missing transverse energy at the cern pp collider. *Physics Letters B*, 122(5):476–485, 1983.
- [7] P. Bagnaia et al. Evidence for $Z^0 \rightarrow e^+e^-$ at the CERN $\bar{p}p$ Collider. *Phys. Lett. B*, 129:130–140, 1983.
- [8] ATLAS Collaboration. Observation of a new particle in the search for the standard model higgs boson with the atlas detector at the lhc. *Physics Letters B*, 716(1):1–29, 2012.
- [9] Cássio Vieira and Antonio Videira. Carried by history: Cesar lattes, nuclear emulsions, and the discovery of the pi-meson. *Physics in Perspective*, 16, 02 2014.
- [10] J Blietschau, Herbert Grässler, W Krenz, D Lanske, R Schulte, H H Seyfert, Klaus Böckmann, P Checchia, C Geich-Gimbel, H G Heilmann, T P Kokott, B Nellen, R Pech, Peter C Bosetti, Vanna T Cocconi, Bianca Conforto, Donald C Cundy, A Grant, Dieter Haidt, P O Hulth, J Von Krogh, Douglas Robert Ogston Morrison, L Pape, Charles Peyrou, H Saarikko, P Schmid, W G Scott, Errietta Simopoulou, Anna Vayaki, H W Wachsmuth, E De Wolf, Michael Aderholz, N Schmitz, Ronald Settles, Karl-Ludwig Wernhard, W Wittek, P Cartwright, R Giles, P Grossmann, R McGow, Gerald Myatt, Donald Hill Perkins, D Radojcic, P B Renton, and B Saitta. Production of charmed mesons in neutrino interactions in hydrogen. *Phys. Lett. B*, 86:108–114. 15 p, Jun 1979.
- [11] Claus Grupen and Boris Shwartz. *Particle Detectors*. Cambridge Monographs on Particle Physics, Nuclear Physics and Cosmology. Cambridge University Press, 2 edition, 2008.
- [12] Rudolf Frühwirth and Are Strandlie. *Pattern Recognition, Tracking and Vertex Reconstruction in Particle Detectors*. Particle Acceleration and Detection. Cham: Springer International Publishing AG., 01 2021.

- [13] B Abelev et al. Technical design report for the upgrade of the ALICE inner tracking system. *Journal of Physics G: Nuclear and Particle Physics*, 41(8):087002, jul 2014.
- [14] M. Šuljić. ALPIDE: the monolithic active pixel sensor for the ALICE ITS upgrade. *Journal of Instrumentation*, 11(11):C11025–C11025, nov 2016.
- [15] P.A. Zyla et al. Review of Particle Physics. *PTEP*, 2020(8):083C01, 2020. and 2021 update.
- [16] ALICE Collaboration. Upgrade of the ALICE Experiment: Letter of Intent. Technical Report CERN-LHCC-2012-012. LHCC-I-022. ALICE-UG-002, CERN, Geneva, Aug 2012.
- [17] K. Aamodt et al. The ALICE experiment at the CERN LHC. *JINST*, 3:S08002, 2008.
- [18] P Buncic, M Krzewicki, and P Vande Vyvre. Technical Design Report for the Upgrade of the Online-Offline Computing System. Technical Report CERN-LHCC-2015-006. ALICE-TDR-019, Apr 2015.
- [19] Alessandro Ferretti. The ALICE Experiment Upgrades. *arXiv preprint arXiv:2201.08871*, 2022.
- [20] Edmundo Garcia-Solis. Perspectives of the ALICE Experiment and Detector Upgrade. *Nucl. Part. Phys. Proc.*, 267-269:382–391, 2015.
- [21] Addendum of the Letter of Intent for the upgrade of the ALICE experiment : The Muon Forward Tracker. Technical report, CERN, Geneva, Aug 2013.
- [22] Betty Bezverkhny Abelev et al. Performance of the ALICE Experiment at the CERN LHC. *Int. J. Mod. Phys. A*, 29:1430044, 2014.
- [23] P Antonioli, A Kluge, and W Riegler. Upgrade of the alice readout amp; trigger system. Technical report, Sep 2013. Presently we require a LHCC-TDR reference number.a later stage we will fill the required information.
- [24] Livia Terlizzi. The ALICE Muon IDentifier. *JINST*, 15:C10031. 8 p, May 2020. Proceeding of the 15th Workshop on Resistive Plate Chambers and Related Detectors (RPC2020), 10-14 February 2020, University of Roma Tor Vergata, Italy.
- [25] Rudolf Frühwirth, Meinhard Regler, Rudolf K Bock, H Grote, D Notz, Meinhard Regler, and Rudolf Frühwirth. *Data analysis techniques for high-energy physics; 2nd ed.* Cambridge monographs on particle physics, nuclear physics, and cosmology. Cambridge Univ. Press, Cambridge, 2000.
- [26] A. Strandlie and W. Wittek. Derivation of jacobians for the propagation of covariance matrices of track parameters in homogeneous magnetic fields. *Nuclear Instruments and Methods in Physics Research Section A: Accelerators, Spectrometers, Detectors and Associated Equipment*, 566(2):687 – 698, 2006.
- [27] Technical Design Report for the Muon Forward Tracker. Technical Report CERN-LHCC-2015-001. ALICE-TDR-018, Jan 2015.

- [28] Z. Drasal and W. Riegler. An extension of the gluckstern formulae for multiple scattering: Analytic expressions for track parameter resolution using optimum weights. *Nuclear Instruments and Methods in Physics Research Section A: Accelerators, Spectrometers, Detectors and Associated Equipment*, 910:127–132, dec 2018.
- [29] M. Hansroul, H. Jeremie, and D. Savard. Fast circle fit with the conformal mapping method. *Nuclear Instruments and Methods in Physics Research Section A: Accelerators, Spectrometers, Detectors and Associated Equipment*, 270(2):498–501, 1988.
- [30] Marcos Antônio Oliveira Derós. Estudo dos limites de detecção de sensores monolíticos de pixéis ativos para o regime de íons de 4 a 100 mev e seu potencial para análise por feixe de íons. LUME UFRGS, 2022.
- [31] Pierre Billoir. Track Fitting With Multiple Scattering: A New Method. *Nucl. Instrum. Meth. A*, 225:352–366, 1984.
- [32] Ivan Kisel. Advances in tracking and trigger concepts. *Journal of Physics: Conference Series*, 523:012022, 06 2014.
- [33] R. Frühwirth. Application of kalman filtering to track and vertex fitting. *Nuclear Instruments and Methods in Physics Research Section A: Accelerators, Spectrometers, Detectors and Associated Equipment*, 262(2):444 – 450, 1987.
- [34] Are Strandlie and Rudolf Frühwirth. Track and vertex reconstruction: From classical to adaptive methods. *Rev. Mod. Phys.*, 82:1419–1458, May 2010.
- [35] Tommaso Toffoli and Norman Margolus. *Cellular Automata Machines: A New Environment for Modeling*. MIT Press, Cambridge, MA, USA, 1987.

APENDICE A

TRACK FINDING IN THE MUON FORWARD TRACKER

This appendix brief overviews the track finding procedure applied in the Muon Forward Tracker (MFT) track reconstruction; a complete explanation and performance studies can be found in MFT's Technical Design Report[27].

MFT track finding combines two algorithms: for tracks with “high” *momentum*, where the curvature of the track can be neglected, the Linear Track Finder (LTF) is applied. To handle lower *momentum* tracks an algorithm based in a Cellular Automaton^[35] (CA) is used. The LTF is applied prior to the CA method, so the later could process low moment tracks lost by the linear algorithm. The LTF is a rather straightforward method: a straight line, called a seed, is created using the two farthest hits with a direction compatible with the vertex, then the candidate is created from the minimization of the distance of the another clusters to the seed line, where the number of clusters are limited by a radius cut. The remaining hits not used in LTF are then used in the CA-based algorithm. The CA algorithm builds a candidate by creating and incrementing a cell, which is a segment connecting two clusters. Both steps are based on selection criteria as radius cut (position and angle ranges) and compatibility with vertex (direction). For each pair of detection planes, the CA tries every combination of clusters within the defined criteria, so it is considerably slower than LTF. On the other hand it tolerates better deviations from a straight line, so its use is appropriate for low *momentum* tracks. Studies using the presented setting - LTF + CA - have shown a good efficiency for track finding at the MFT detector¹.

¹https://indico.cern.ch/event/391595/contributions/936092/attachments/783738/1074395/MFT_Plenary_Lyon_StandTrack.pdf

APENDICE B

TRANSFORMATIONS BETWEEN MFT AND MCH COORDINATE SYSTEMS

MFT and MCH coordinate systems

In this section, the parameters used in the MFT coordinate system and MCH coordinate system are described. The five parameters on both coordinate systems are referred to as x_i and α_i for the MFT and MCH, respectively.

Description of the MFT Coordinate System

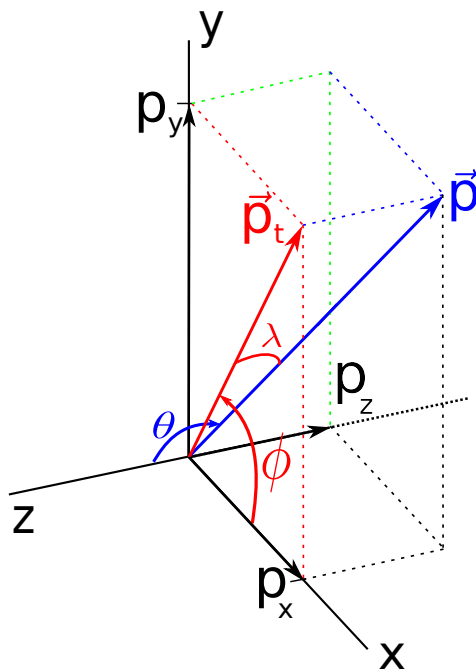


Figure 21: Track orientation angles on the MFT coordinate system. Solid black lines indicate axes positive directions. λ is negative for tracks moving towards the MFT.

MFT standalone tracking uses the following coordinate system: $\{x, y, \phi, \tan \lambda, (q/p_t)\}$, as shown in figure 21. Defining

- $x_0 = x$: Cartesian x coordinate;

- $x_1 = y$: Cartesian y coordinate;
- $x_2 = \phi$: direction of p_t on the xy-plane; the azimuthal projection of the momentum vector on the transverse plane.
- $x_3 = \tan \lambda$: λ is complementary to the polar angle θ , i.e., $\lambda = \frac{\pi}{2} - \theta$; Also, $\tan \lambda = \cot \theta$.
- $x_4 = q/p_t$: charged inverse transverse *momentum*. Charge in natural units: charge of particle is the sign of q/p_t .

let us represent the MFT parameters state vector as $\{x_0, x_1, x_2, x_3, x_4\}$.

Description of the MCH Coordinate System

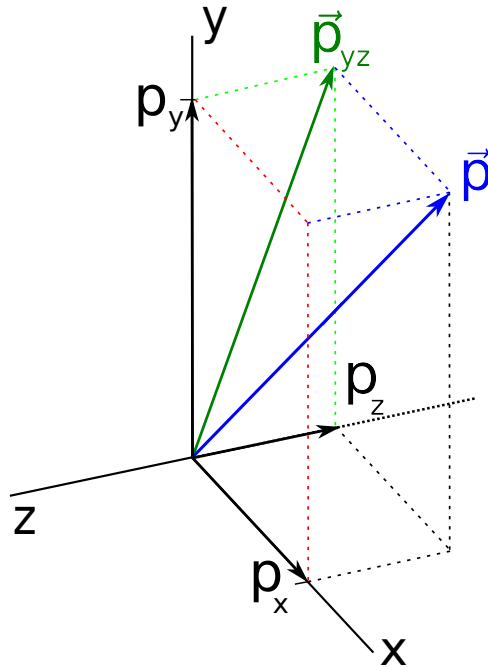


Figure 22: Momentum \vec{p} and bending Momentum p_{yz} on the MCH coordinate system. Solid black lines indicate the axes positive directions.

The set of coordinates of MCH system is: $\{x, \text{SlopeX}, y, \text{SlopeY}, q/p_{yz}\}$. The coordinates are showed in figure 22 and are defined bellow:

- $\alpha_0 = x$: Cartesian x coordinate; “a.k.a.“ *Non Bending Coordinate*;
- $\alpha_1 = \text{SlopeX} = \frac{p_x}{p_z}$, “a.k.a.“ *Non Bending Slope* ;
- $\alpha_2 = y$: Cartesian y coordinate; “a.k.a.“ *Bending Coordinate*;
- $\alpha_3 = \text{SlopeY} = \frac{p_y}{p_z}$, “a.k.a.“ *Bending Slope* ;

- $\alpha_4 = q/p_{yz}$: Charged inverse bending *Momentum*. The Bending *momentum* is the projection of the total *momentum* p on the yz -plane. Charge in natural units.

which let us represent the state of MCH tracks as: $\{\alpha_0, \alpha_1, \alpha_2, \alpha_3, \alpha_4\}$.

A figure showing the *momenta* relations and angles is presented in figure 23.

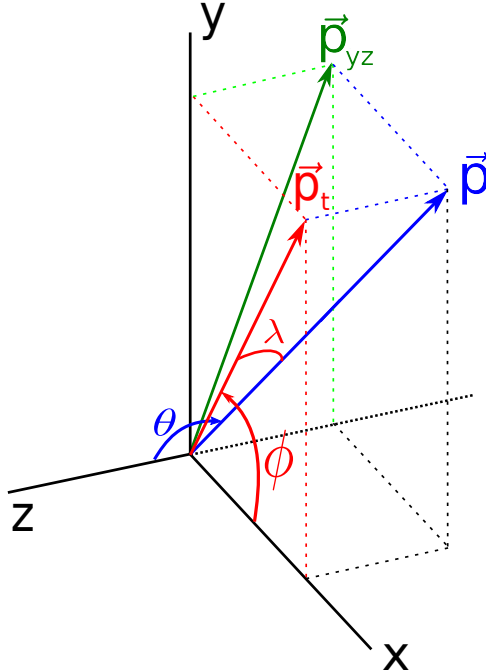


Figure 23: Illustration of *momentum* \vec{p} , its projections \vec{p}_{yz} and \vec{p}_t and the angles θ , ϕ and λ . Solid black lines indicate axes positive directions. λ is negative for tracks moving towards the MFT.

It is noteworthy that ALICE's Muon Arm is positioned along the negative side of the z . Thus, tracks originated in the center of the ALICE detector are observed with a negative z component of \vec{p} . Therefore $\theta > 90^\circ$ and $\lambda < 0$.

Useful expressions on the MFT and MCH coordinate systems

The following expressions implemented in ALICE O2 MFT and MCH tracking classes are used for the conversion between the MFT and MCH coordinate systems:

***Momentum* equations in the MFT coordinate system**

$$p_x = p_t \cos \phi = \frac{\cos \phi}{|q/p_t|} = \frac{\cos x_2}{|x_4|} \quad (\text{B.1})$$

$$p_y = p_t \sin \phi = \frac{\sin \phi}{|q/p_t|} = \frac{\sin x_2}{|x_4|} \quad (\text{B.2})$$

$$p_z = p_t \tan \lambda = \frac{\tan \lambda}{|q/p_t|} = \frac{x_3}{|x_4|} \quad (\text{B.3})$$

$$p = p_t \sqrt{1 + \tan^2 \lambda} = \frac{\sqrt{1 + \tan^2 \lambda}}{|q/p_t|} = \frac{\sqrt{1 + (x_3)^2}}{|x_4|} \quad (\text{B.4})$$

$$p = \frac{p_t}{\cos \lambda} = \frac{1}{|q/p_t| \cos \lambda} = \frac{1}{|x_4| \cos \lambda} \quad (\text{B.5})$$

$$p = \frac{p_z}{\sin \lambda} \quad (\text{B.6})$$

Momentum equations in the MCH coordinate system

$$p_z = \frac{-p_{yz}}{\sqrt{1 + \text{SlopeY}^2}} = \frac{-1}{|q/p_{yz}| \sqrt{1 + \text{SlopeY}^2}} = \frac{-1}{|\alpha_4| \sqrt{1 + \alpha_3^2}} \quad (\text{B.7})$$

$$p_x = p_z \text{SlopeX} = p_z \alpha_1 \quad (\text{B.8})$$

$$p_x = \frac{-\text{SlopeX}}{|q/p_{yz}| \sqrt{1 + \text{SlopeY}^2}} = \frac{-\alpha_1}{|\alpha_4| \sqrt{1 + \alpha_3^2}} \quad (9.1)$$

$$p_y = p_z \text{SlopeY} = p_z \alpha_3 \quad (\text{B.9})$$

$$p_y = \frac{-\text{SlopeY}}{|q/p_{yz}| \sqrt{1 + \text{SlopeY}^2}} = \frac{-\alpha_3}{|\alpha_4| \sqrt{1 + \alpha_3^2}} \quad (10.1)$$

$$p = -p_z \sqrt{1 + \text{SlopeY}^2 + \text{SlopeX}^2} = \frac{\sqrt{1 + \text{SlopeY}^2 + \text{SlopeX}^2}}{|q/p_{yz}| \sqrt{1 + \text{SlopeY}^2}} = \frac{\sqrt{1 + \alpha_3^2 + \alpha_1^2}}{|\alpha_4| \sqrt{1 + \alpha_3^2}} \quad (\text{B.10})$$

The transverse and bending momentum in the MFT and MCH are obtained from their respective coordinate systems by $p_t = \left| \frac{1}{q/p_t} \right|$ and $p_{yz} = \left| \frac{1}{q/p_{yz}} \right|$.

Relations between Cartesian, MFT, and MCH coordinate systems.

Using the definitions of section* B, the following relations are used hereafter:

MFT

$$p_x = \frac{\cos x_2}{|x_4|} \quad (\text{A1})$$

$$p_y = \frac{\sin x_2}{|x_4|} \quad (\text{A2})$$

$$p_z = \frac{x_3}{|x_4|} \quad (\text{A3})$$

$$p = \frac{\sqrt{1 + (x_3)^2}}{|x_4|} \quad (\text{A4})$$

$$p = \frac{1}{|x_4| \cos \lambda} \quad (\text{A4.1})$$

$$p = \frac{p_z}{\sin \lambda} \quad (\text{A4.2})$$

MCH

$$p_x = p_z \alpha_1 \quad (\text{B1})$$

$$p_y = p_z \alpha_3 \quad (\text{B2})$$

$$p_z = \frac{-1}{|\alpha_4| \sqrt{1 + \alpha_3^2}} \quad (\text{B3})$$

$$p_x = \frac{-\alpha_1}{|\alpha_4| \sqrt{1 + \alpha_3^2}} \quad (\text{B1.1})$$

$$p_y = \frac{-\alpha_3}{|\alpha_4| \sqrt{1 + \alpha_3^2}} \quad (\text{B2.1})$$

$$p = \frac{\sqrt{1 + \alpha_3^2 + \alpha_1^2}}{|\alpha_4| \sqrt{1 + \alpha_3^2}} \quad (\text{B4})$$

X, Y and Z coordinates

In both MFT and MCH coordinate systems the positions are given by the X, Y and Z Cartesian coordinates:

$$X_{MFT} = X_{MCH} = X \quad (\text{B.11})$$

$$Y_{MFT} = Y_{MCH} = Y \quad (\text{B.12})$$

Transformations from MCH to MFT coordinate system

$$\phi = f(\text{SlopeX}, \text{SlopeY})$$

The direction of the p_t on the MFT coordinate system depends only on MCH's SlopeX and SlopeY.

We begin by isolating $\cos x_2$ in equation (A1) and substituting p_x with (B1):

$$\cos x_2 = p_z \alpha_1 |x_4| \quad (\text{B.13})$$

now substituting p_z with (B3):

$$\cos x_2 = -\frac{\alpha_1 |x_4|}{|\alpha_4| \sqrt{1 + \alpha_3^2}} \quad (\text{B.14})$$

In a similar way, one isolates $\sin x_2$ in (A2) and use (B2) and (B3) to obtain:

$$\sin x_2 = -\frac{\alpha_3 |x_4|}{|\alpha_4| \sqrt{1 + \alpha_3^2}} \quad (\text{B.15})$$

Dividing (B.15) by (B.14) let us write x_2 as:

$$x_2 = \text{atan}2(-\alpha_3, -\alpha_1)^1 \quad (\text{B.16})$$

Contrary to the usual *atan* function, here it is mandatory to keep the negative signs to obtain the correct quadrant since *atan2*¹ considers the signs of both arguments to determine the quadrant of the resulting angle. The quantities α_1 and α_3 have opposite signs in relation to p_x and p_y , respectively.

$$q/p_t = f(\text{SlopeX}, \text{SlopeY}, q/p_{yz})$$

First we substitute $x_3 = |x_4|p_z$ in (A4):

$$p = \frac{\sqrt{1 + (|x_4|p_z)^2}}{|x_4|} \quad (\text{B.17})$$

Isolating $|x_4|$:

$$|x_4| = (p^2 - p_z^2)^{-1/2} \quad (\text{B.18})$$

Using (B4) we can re-write this equation as:

$$|x_4| = \left(p_z \sqrt{\alpha_3^2 + \alpha_1^2} \right)^{-1} \quad (\text{B.19})$$

¹*atan2* is a C++ function, equivalent to the trigonometric function *arctan*: *atan2(x,y)* := *arctan(x,y)*. For more see: <http://www.cplusplus.com/reference/cmath/atan2/>

And finally, with (B3) we get:

$$|x_4| = \left(\frac{\sqrt{\alpha_3^2 + \alpha_1^2}}{|\alpha_4| \sqrt{1 + \alpha_3^2}} \right)^{-1} = \frac{|\alpha_4| \sqrt{1 + \alpha_3^2}}{\sqrt{\alpha_3^2 + \alpha_1^2}} \quad (\text{B.20})$$

The particle charge q on both coordinate systems is obtained from the sign of x_4 and α_4 . Since both x_4 and α_4 have equal the sign for a given track, it is possible to remove the absolute value operators, which results in

$$x_4 = \frac{\alpha_4 \sqrt{1 + \alpha_3^2}}{\sqrt{\alpha_3^2 + \alpha_1^2}} \quad (\text{B.21})$$

$$\tan \lambda = f(\text{Slope}X, \text{Slope}Y)$$

To obtain $x_3(\tan \lambda)$ one has to isolate x_3 at (A3) and combine with (B3) and (B.20) to get:

$$x_3 = p_z |x_4| = -\frac{1}{\sqrt{\alpha_3^2 + \alpha_1^2}} \quad (\text{B.22})$$

Transformations from MFT to MCH coordinate system

$$\text{Slope}X = g(\phi, \tan \lambda)$$

For α_1 (SlopeX) let us use p_x from (A1) and (B1):

$$p_x = \frac{\cos x_2}{|x_4|} = p_z \alpha_1 \quad (\text{B.23})$$

Now substitute (A3) into the above equation and isolate α_1 :

$$\alpha_1 = \frac{\cos x_2}{x_3} \quad (\text{B.24})$$

$$\text{Slope}Y = g(\phi, \tan \lambda)$$

In a similar way as section B, lets use p_y from (A2) and (B2) to find α_3 (SlopeY). Applying (A3) one obtains:

$$\alpha_3 = \frac{\sin x_2}{x_3} \quad (\text{B.25})$$

$$q/p_{yz} = g(\phi, \tan \lambda, q/p_t)$$

Consider the total track momentum on both MFT and MCH coordinate systems. Combining (A4) and (B4) yields

$$\frac{\sqrt{1+x_3^2}}{|x_4|} = \frac{\sqrt{1+\alpha_3^2 + \alpha_1^2}}{|\alpha_4| \sqrt{1+\alpha_3^2}} \quad (\text{B.26})$$

Using with (B.24) and (B.25) and reordering the terms we get:

$$\frac{\sqrt{1+x_3^2}}{|x_4|} = \frac{\sqrt{1+x_3^2}}{x_3 |\alpha_4| \sqrt{1+\alpha_3^2}} \quad (\text{B.27})$$

Using (B.25) once more for α_3 we can write:

$$|x_4| = x_3 |\alpha_4| \sqrt{1 + (\sin^2 x_2)/x_3^2} \quad (\text{B.28})$$

Finally, isolating $|\alpha_4|$:

$$|\alpha_4| = \frac{|x_4|}{\sqrt{x_3^2 + \sin^2 x_2}} \quad (\text{B.29})$$

As in eq. (B.21), α_4 and x_4 have the same sign, thus

$$\alpha_4 = \frac{x_4}{\sqrt{x_3^2 + \sin^2 x_2}} \quad (\text{B.30})$$

Summary

This section summarizes the equations used to transform between MFT and MCH coordinate systems.

Transformations from MCH to MFT

$$X_{MFT} = X_{MCH} \quad (\text{B.11})$$

$$Y_{MFT} = Y_{MCH} \quad (\text{B.12})$$

$$x_2 = \text{atan2}(-\alpha_3, -\alpha_1) \quad (\text{B.16})$$

$$x_3 = -\frac{1}{\sqrt{\alpha_3^2 + \alpha_1^2}} \rightarrow \tan \lambda = -\frac{1}{\sqrt{\text{Slope}Y^2 + \text{Slope}X^2}} \quad (\text{B.22})$$

$$x_4 = \frac{\alpha_4 \sqrt{1 + \alpha_3^2}}{\sqrt{\alpha_3^2 + \alpha_1^2}} \rightarrow \frac{q}{p_t} = \frac{q}{p_{yz}} \frac{\sqrt{1 + \text{Slope}Y^2}}{\sqrt{\text{Slope}Y^2 + \text{Slope}X^2}} \quad (\text{B.21})$$

Transformations from MFT to MCH

$$X_{MCH} = X_{MFT} \quad (\text{B.11})$$

$$Y_{MCH} = Y_{MFT} \quad (\text{B.12})$$

$$\alpha_1 = \frac{\cos x_2}{x_3} \rightarrow \text{Slope}X = \frac{\cos \phi}{\tan \lambda} \quad (\text{B.24})$$

$$\alpha_3 = \frac{\sin x_2}{x_3} \rightarrow \text{Slope}Y = \frac{\sin \phi}{\tan \lambda} \quad (\text{B.25})$$

$$\alpha_4 = \frac{x_4}{\sqrt{x_3^2 + \sin^2 x_2}} \rightarrow \frac{q}{p_{yz}} = \frac{q}{p_t} \frac{1}{\sqrt{\tan^2 \lambda + \sin^2 \phi}} \quad (\text{B.30})$$

Jacobians

Jacobians necessary to transform the covariance matrix between the MFT and MCH coordinate systems are presented bellow. Python's sympy package was used in a *Jupyter Notebook*¹ in order to perform the calculations and obtain the Jacobians.

MCH coordinate system to MFT coordinate system

$$\begin{bmatrix} 1 & 0 & 0 & 0 & 0 \\ 0 & 0 & 1 & 0 & 0 \\ 0 & -\frac{\alpha_3}{\alpha_1^2 + \alpha_3^2} & 0 & \frac{\alpha_1}{\alpha_1^2 + \alpha_3^2} & 0 \\ 0 & \frac{\alpha_1}{(\alpha_1^2 + \alpha_3^2)^{\frac{3}{2}}} & 0 & \frac{\alpha_3}{(\alpha_1^2 + \alpha_3^2)^{\frac{3}{2}}} & 0 \\ 0 & -\frac{\alpha_1 \alpha_4 \sqrt{\alpha_3^2 + 1}}{(\alpha_1^2 + \alpha_3^2)^{\frac{3}{2}}} & 0 & \frac{\alpha_3 \alpha_4 \sqrt{\alpha_3^2 + 1}}{(\alpha_1^2 + \alpha_3^2)^{\frac{3}{2}}} & \frac{\sqrt{\alpha_3^2 + 1}}{\sqrt{\alpha_1^2 + \alpha_3^2}} \end{bmatrix}$$

MFT coordinate system to MCH coordinate system

$$\begin{bmatrix} 1 & 0 & 0 & 0 & 0 \\ 0 & 0 & -\frac{1}{x_3} \sin(x_2) & -\frac{1}{x_3^2} \cos(x_2) & 0 \\ 0 & 1 & 0 & 0 & 0 \\ 0 & 0 & \frac{1}{x_3} \cos(x_2) & -\frac{1}{x_3^2} \sin(x_2) & 0 \\ 0 & 0 & -\frac{x_4 \sin(x_2) \cos(x_2)}{(x_3^2 + \sin^2(x_2))^{\frac{3}{2}}} & -\frac{x_3 x_4}{(x_3^2 + \sin^2(x_2))^{\frac{3}{2}}} & \frac{1}{\sqrt{x_3^2 + \sin^2(x_2)}} \end{bmatrix}$$

¹<https://jupyter.org/install.html>

Acronyms

Symbols

η pseudo-rapidity.

p_t transverse *momentum*.

A

ALICE O² ALICE online-offline system.

ALICE A Large Ion Collider Experiment.

ALPIDE ALICE PIxel DEtector.

C

CA Cellular Automaton.

CERN Conseil Européen pour la Recherche Nucléaire (European Council for Nuclear Research).

F

FCF Fast Circle Fit.

G

GeV Giga electronvolt (10^9 electronvolts).

K

KF Kalman Filter.

L

LHC Large Hadron Collider.

LS 2 Long shutdown 2.

LTF Linear Track Finder.

M

MAPS Monolithic Active Pixel Sensor.

MCH Muon Tracking Chambers.

MCS Multiple Coulomb Scattering.

MeV Mega electronvolt (10^6 electronvolts).

MFT Muon Forward Tracker.

MID Muon Identifier.

MWPC Multi-wire proportional chamber.

Q

QCD Quantum chromodynamics.

QGP Quark-Gluon Plasma.

T

TeV Tera electronvolt (10^{12} electronvolts).

TPC Time-Projection Chamber.

Glossary

Symbols

Υ meson composed of a bottom quark and a anti-bottom quark. Also known as *bottomonium*.
8, 9

J/ψ meson composed of a charm quark and a anti-charm quark. Also known as *charmonium*.
8–12

C

center-of-mass energy energy measured in the center-of-mass reference frame (frame where the total *momentum* of the system is zero). In experiments with colliding beams, the center of mass energy is the sum of the energy (of the particle) of the two beams. 5

H

H dibaryon Proposed hexaquark composed of two up quarks, two down quarks and two strange quarks. 8

I

interaction point position where particles collide. In a circular collider, as the LHC, is the point where the opposing circulating beams collide head-on. 9, 11, 36

invariant mass equals to the mass of a particle in its rest frame. This quantity is the same in all frames of reference. In natural units is defined as: $m_0^2 = E^2 - |\mathbf{p}|$, where E is the particle's energy and \mathbf{p} its *momentum*. 9

M

MINUIT MINUIT – Function Minimization and Error Analysis - is a numerical minimization software library widely used in particle physics. 27

O

open beauty a meson which has beauty property, i.e. beauty quantum number different from zero. 10

open charm a meson which has charm property, i.e. charm quantum number different from zero. 10

P

primary vertex usually used as a synonym of *interaction point*, i.e., the point where two particle beams collide. 4, 8, 11

pseudo-rapidity Common spatial coordinate used to describe the angle of a particle in respect to the beam axis. It is defined as $\eta \equiv -\ln \tan(\theta/2)$, where θ is the angle between a particle's *momentum* and the beam axis. 8, 9, 11, 32, 35

Q

Quark-Gluon Plasma State in which it is believed the universe was around 10^{10} s to 10^6 s after the Big Bang. In this state of high energy density, the quarks and gluons that compose the baryonic matter are freed of their strong interaction, i.e., quarks are *deconfined*. 1

quarkonia A quarkonium (pl. quarkonia) is a meson constituted by a quark and its own anti-quark. The J/ψ meson (charmonium) and Υ meson (bottomonium) are examples of quarkonia. 8, 9

R

radiation length Mean distance over which a charged particle has to travel inside a material to have its energy reduced by a factor of $1/e$. 10, 21, 22, 37, 43, 44, 46

ROOT Data Analysis Framework framework for data processing, aimed for particle physics.
27

RUN 3 Third period of data taking at CERN's LHC. 7, 11

S

secondary vertices point where an unstable particle decays after moving away of the interaction point. 4, 9

T

transverse momentum Component of the *momentum* perpendicular to the beam axis. For ALICE: $p_t = \sqrt{p_x^2 + p_y^2}$. 1, 7, 10, 15, 16, 24, 31, 32, 36, 39–41, 44, 46